Characterization of Cellular Metabolism throughout the Cell Cycle in Cancer: An Integrated Experimental-Computational Approach

Eunyong Ahn

Characterization of Cellular Metabolism throughout the Cell Cycle in Cancer: An Integrated Experimental-Computational Approach

Research thesis

In Partial Fulfillment of the Requirements for the Degree of Doctor of Philosophy

Eunyong Ahn

Submitted to the Senate of the Technion - Israel Institute of Technology

CHESHVAN, 5779, Haifa, October 2018

The Research Thesis or Project Thesis or Final Paper Was Done Under the Supervision of Prof. Tomer Shlomi in the Faculty of Computer Science

Some results in this thesis have been published in an article by the author and research collaborators:

Temporal fluxomics reveals oscillations in TCA cycle flux throughout the mammalian cell cycle, E. Ahn, P. Kumar, D. Mukha, A. Tzur, T. Shlomi, Molecular systems biology 13 (11), 953

Some of the experiments involving cell synchronization were performed together with P. Kumar; D. Mukha assisted with LC-MS sample analysis; A. Tzur participated in the research design.

Table of Contents

List of Figures

Abstract

Cell cycle progression is tightly interlinked with cellular metabolism. The availability of sufficient metabolic nutrients and intracellular energy status control the ability of cells to enter and progress through cell cycle. While the cell cycle machinery was found to regulate the concentration of key metabolic enzymes, an understanding of how the actual rate of metabolic reactions and pathway (i.e. metabolic flux) change throughout the cell cycle is still fundamentally missing. Here, we developed a temporal-fluxomics approach to derive a comprehensive and quantitative view of alterations in metabolic fluxes throughout the mammalian cell cycle. This is achieved by combining pulse-chase LC-MS based isotope tracing in synchronized cell populations with computational deconvolution and metabolic flux modelling. Specifically, we synchronized HeLa cells and applied high-throughput LC-MS based targeted metabolomics analysis to synchronized cell populations throughout two complete cell cycles. As cell synchronization is gradually lost with time due to inherent non-genetic cell-to-cell variability, the distribution of cell cycle phases in the synchronized cell population becomes similar to that of non-synchronized cells with time. To account for the loss of synchrony and to precisely quantify oscillations in metabolite levels, we employed "computational synchronization". Inferring the dynamics of metabolite concentrations throughout the cell cycle (rather than that of metabolite abundances) further required estimates of the dynamics of cell volume throughout the cell cycle. Finally, a variant of Kinetic Flux Profiling (KFP) was employed to infer metabolic flux dynamics throughput the cell cycle.

Applied to HeLa cells, we derived a first comprehensive and quantitative view of metabolic flux oscillations at a high temporal resolution in central metabolism throughout the cell cycle of human cells, showing complementary oscillations between glucose and glutamine-derived flux in the TCA cycle throughout the cell cycle: oxidation of glucose-derived flux

peaks in late G1 phase while oxidative and reductive glutamine metabolism dominates S phase. These complementary flux oscillations maintain a constant production rate of reducing equivalents and oxidative phosphorylation flux throughout the cell cycle. The shift from glucose to glutamine oxidation in S phase plays an important role in cell cycle progression and cell proliferation. After treating HeLa cells with the PDK inhibitor DCA, the oscillations in glucose flux into TCA cycle were eliminated, suggesting that cell cycle specific regulation of PDH activity may be involved in regulating these flux oscillations.

Understanding the metabolic adaptation of cells to tumorigenic mutations is a central goal of cancer metabolic research. Considering that tumorigenic mutations typically alter cell cycle progression, flux alterations observed at a cell population level may merely reflect a change in the distribution of cell-cycle phases in the population (due to cells in different phases having different metabolic fluxes). Hence, the presented temporal-fluxomics approach will enable to revisit our understanding of oncogene-induced metabolic alterations, disentangling population level artifacts from directly regulated flux alterations with important tumorigenic role and revealing potential targets for therapy.

List of symbols and abbreviations

NADH - Nicotinamide Adenine Dinucleotide Hydrate

FADH - Flavin Adenine Dinucleotide Hydrate

ATP - Adenosine Triphosphate

ADP - Adenosine Diphosphate

PPP - Pentose Phosphate Pathway

MFA - Metabolic Flux Analysis

LC-MS - Liquid Chromatography–Mass Spectrometry

[U-^{13}C] - Uniformly ^{13}C labeled

HK - the protein symbol for hexokinase

PFK - the protein symbol for phosphofructokinase

GLS - the protein symbol for glutaminase

PRPS2 - the protein symbol for phosphoribosyl pyrophosphate synthetase

CAD - the protein symbol for carbamoyl-phosphate synthetase 2

SDH **-** the protein symbol for succinate dehydrogenase

FH - the protein symbol for fumarate hydratase

JHDM - the protein symbol for jumonji domain-containing histone demethylase

TET - the protein symbol for ten-eleven-translocation protein

IDH1/2 - the protein symbol for isocitrate dehydrogenase 1/2

2-HG - the protein symbol for D-2-hydroxyglutarate

ESI - Electrospray Ionization

13C –MFA - ^{13}C-Metabolic Flux Analysis

13C-NMFA - Isotopic non steady state 13C-Metabolic Flux Analysis

DMFA - Dynamic Metabolic Flux Analysis

13C-DMFA - ^{13}C-Dynamic Metabolic Flux Analysis

AMPK - the gene coding AMP-activated protein kinase

mTOR - the Mammalian Target of Rapamycin

ACL - the protein symbol for ATP citrate lyase

PD - the protein symbol for pyruvate dehydrogenase

CDK - the protein symbol for cyclin-dependent kinase

APC/C - the protein symbol for anaphase-promoting complex/cyclosome

SCF - the protein symbol for Skp1/cullin/F-box

CCE - Countercurrent Centrifugal Elutriation

FACS - Fluorescence-Activated Cell Sorting

1. Introduction

1.1 Cancer Metabolism

Cancer is a major global health problem: ~1.7 million new cases are projected to occur in 2018 worldwide [4]. While major research advancements have been made in cancer research, extensive variation in survival between cancer types still exists [4]. Although cancer death rates have decreased in recent decades, for some cancers, death rates have remained stubbornly constant, or even have risen [4,5]. Recently, there is a major resurgence of interest in the field of cancer metabolism due to several advancements in this field [6,7]: (i) The metabolic rewiring in cancer cells spans many pathways and goes much beyond the sole induction of aerobic glycolysis; (ii) tumor suppressors and oncogenes within growth-factor signaling pathways directly regulate the activity of a variety of metabolic pathways; and (iii) oncogenic mutations found in several metabolic enzymes in specific cancers. Research in this field has demonstrated that metabolic alterations in cancer cells are a potential therapeutic target for a variety of cancers [8–11].

1.1.1. The metabolic rewiring in cancer cells

Cancer adapts its metabolism to support abnormal demand for the growth even under oxygen or nutrient-depleted conditions. Furthermore, it maintains its viability and homeostasis to counteract the metabolic alteration during tumorigenesis[12]. While normal cells would not be able to withstand cancer environment, cancer cells are reprogrammed to survive and promote proliferation through its adapted metabolism. The hallmarks of rewired cancer metabolism are summarized on the basis of the review written by Pavlova & Thompson, in 2016[12] (Table 1).

Table 1: The hallmarks of rewired cancer metabolism[12]. Cancer cell alters its pathway to support the high energy and biomass demand even under nutrient and oxygen depleted

condition. This rewired cancer metabolism can be categorized as following 6 specific changes: 1. Deregulated uptake of glucose and amino acids, 2. Use of opportunistic modes of nutrient acquisition, 3. Use of glycolysis/TCA cycle intermediates for biosynthesis and NADPH production, 4. Increased demand for nitrogen (Cancer cell optimize de novo biosynthesis of arginine and does not rely on the exogenous Arginine influx), 5. Alterations in metabolite-driven gene regulation, 6. Metabolic interactions with the microenvironment

Known cancer-associated metabolic changes		Description of alteration	Effect of alteration	References
1. Deregulated uptake of glucose and amino acids	a.	Increased glucose consumption (physiological for normal tissue under hypoxia, Warbug effect)	• Support carbon demand • Support reducing power (NADH, $FADH_2$)	6,13
	b.	Increased glutamine consumption	• Support carbon demand • Support nitrogen demand • Facilitate the AA import as LAT1 substrates (leucine, isoleucine, valine, methionine, tyrosine, tryptophan and phenylalanine)	13,14
2. Use of opportunistic modes of nutrient acquisition	a.	Macropinocytosis stimulated by Ras- and c-Src-driven actin cytoskeleton remodeling.	• Recover free amino acids through the lysosomal degradation of extracellular proteins	15
	b.	The engulfment and digestion of entire living cells via a process known as entosis	• A mutant KRAS allele are more likely to perpetrate entosis than to be consumed in this process	16,17
	c.	Import “ready-made” unsaturated fatty acids	• Supplement for the missing unsaturated fatty acid species induced by hypoxia (biosynthetic reactions that require molecular oxygen as an electron acceptor are suppressed under hypoxia)	18
3. Use of glycolysis/TCA cycle intermediates for biosynthesis	a.	Rate-limiting enzymes within branching pathways of glycolysis are frequently upregulated in tumors	• Increase the production of o Cytosolic acetyl-CoA o One-carbon-carrying folate cycle units o S-adenosylmethionine (SAM) o Fructose-6-phosphate	19,20,13

	and NADPH production			o Dihydroxyacetone phosphate (DHAP) o 3-phosphoglycerate	
		b.	Elevated utilization of PPP	• Support NADPH and ribose-5-phosphate biosynthesis	21,22,23
		c.	Increase lactate production	• Support NAD+ to sustain glycolysis and avoid flooding the mitochondria with a supply of excess NADH	13
4.	Increased demand for nitrogen (Cancer cell optimize *de novo* biosynthesis of arginine and does not rely on the exogenous Arginine influx)	a.	Increased glutamine consumption	• Support purine and pyrimidine production • Support non-essential amino acid production	13
		b.	Increased biosynthesis of asparagine from aspartate, catalyzed by asparagine synthase	• Support nitrogen in conditions of glutamine deprivation	24
		c.	[*tumorigenesis strategy*] Suppression of the arginine synthesis in the urea cycle by argininosuccinate lyase (ASL) and argininosuccinate synthase (ASS1)	• Accumulate ornithine, which is then utilized in the production of polyamines (polyamines have been shown to inhibit apoptosis and promote tumor growth and invasion)	25,26
5.	Alterations in metabolite-driven gene regulation	a.	Increased cytosolic acetyl-CoA	• Acetylate histones and enhance gene expression level • Activate Akt pathway and promote protein synthesis and cell proliferation	13,26
		b.	alterations in SAM and NAD+ levels	• Regulate cytosine methylation on DNA and • Regulate adenosine methylation on mRNA • Regulate sirtuins which catalyze the removal of acetyl marks from histone and non-histone proteins	27,28
		c.	Elevated intracellular levels of fumarate and succinate, or elevated 2-HG (competitive inhibitor of α-ketoglutarate dependent dioxygenases)	• Inhibit dioxygenase and increase DNA methylation • Elevate HIF1α (a TET family of DNA demethylases, Jumonji C family of histone demethylases, mRNA demethylases FTO and ALKBH5,	13,29,30

				and a family of prolyl hydroxylase (PHD) enzymes)	
6.	Metabolic interactions with the microenvironment	a.	Increased extracellular lactate level	• Attenuate dendritic and T cell activation and monocyte migration • Promote immunosuppression via the polarization of resident macrophages • Promote angiogenesis and increase tumor invasiveness • Acidify the cellular micro environment (lactate secretion is coupled to the co-transport of H+)	30,31, 32,33
		b.	Overexpressed tryptophan-degrading dioxygenases indoleamine-2, 3-dioxygenase (IDO1) and tryptophan-2, 3-dioxygenase (TDO2), which catalyze the conversion of an essential amino acid, tryptophan, into kynurenine	• Trigger amino acid deprivation-associated apoptosis of effector T cells • Promote regulatory T-cell phenotype, further contributing to the suppression of antitumor immune responses • Promote the degradation of the extracellular matrix and invasion	34,35,36

1.1.2. Metabolic pathways regulated by tumor suppressors and oncogenes

The PI3K-AKT-mTOR signaling pathway in cancer cells is often up-regulated by the alteration of residing oncogenes and tumor suppressor to maintain the signaling regardless of the stimuli from growth factors. Akt signaling promotes a high level of glucose uptake through the elevated expression of glucose transporter GLUT1 and the relocation of GLUT1 from the endomembranes to the cell surface[37,38]. Besides, Akt further enhances the glycolytic flux through potentiating enzymes, hexokinase (HK) and phosphofructokinase (PFK), catalyzing key irreversible steps in the upstream of glycolysis[37,38]. Kras, oncogene frequently mutated in lung, colon, and pancreatic cancers, also up-regulates glycolysis and activate MYC, the transcription factor frequently amplified in cancer to promote tumorigenicity[39]. A major

role of MYC pathway is regulating glutaminolysis as following, to induce the transcription of glutamine transporters ASCT2 and SN2[39], and to promote the expression of enzymes for glutamine utilization, such as glutaminase (GLS1&2)[40], phosphoribosyl pyrophosphate synthetase (PRPS2)[40] and carbamoyl-phosphate synthetase 2 (CAD)[40]. Moreover, loss of tumor suppressor protein such as TP53 (tumor protein p53), or *Rb* family proteins induce a higher glycolytic flux and fatty acid synthesis, and enhance the glutaminolysis through E2F-dependent upregulation of ASCT2 and GLS1, respectively[40].

1.1.3. Oncogenic mutations found in several metabolic enzymes

Recently, several studies unveil oncogenic contribution of altered metabolism on the basis of the oncogenic mutation of enzymes residing in well-appreciated metabolic pathways. For example, mutations in succinate dehydrogenase (SDH), accumulating succinate, were found in paragangliomas, pheochromocytomas, and a subset of sporadic gastrointestinal stromal tumors[41,42]. Similarly, fumarate hydratase (FH) deficient cells, accumulating fumarate, were found in renal cancer, paragangliomas, and pheochromocytomas[43]. These two mutated metabolic enzyme share a common phenotype because both succinate and fumarate inhibit α-ketoglutarate-dependent dioxygenases activity[43]. They promote hypermethylation of DNA through inhibiting jumonji domain-containing histone demethylase (JHDM) and ten eleven translocation (TET) in DNA methylation pathway[13] (Figure 1a[13]). Also, Prolyl hydroxylase is not capable of degrading HIF1α efficiently, resulting in the elevated level of HIF1α[13]. Other oncogenic mutations, modulating the activity of α-ketoglutarate-dependent dioxygenases, are gain-of-function mutations of isocitrate dehydrogenase 1 (IDH1) and isocitrate dehydrogenase 2 (IDH2)[13]. Unlike normal isocitrate dehydrogenases, converting isocitrate to α-ketoglutarate, mutated IDHs preferentially transform α-ketoglutarate to the D-2-hydroxyglutarate (2-HG), a competitive inhibitor of α-ketoglutarate-dependent dioxygenases[44,45]. Thus, mutatant IDH also drive hypermethylation of DNA and induce the HIF1α signaling pathway (Figure 1b[46]).

(a)

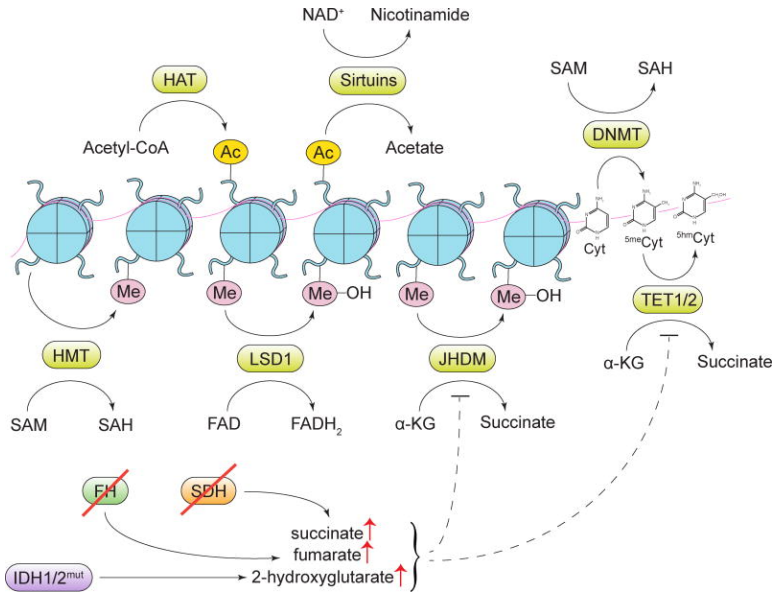

(b)

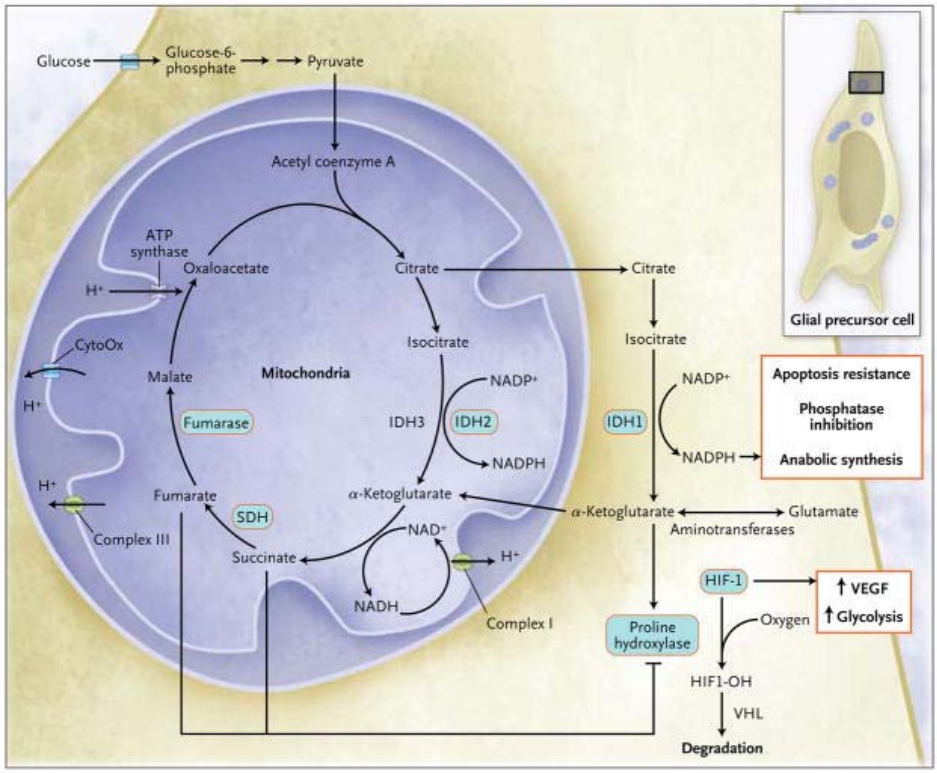

Figure 1: Mutations of several metabolic enzymes residing in mitochondrial TCA cycle and its branched pathway were found in specific cancer types[10,43] (figures are from Pavlova, N. N. & Thompson, C. B, *Cell Metab.*, **23**, 2016 & C. B, *N. Engl. J. Med.,* **360**, 2009). (a) TCA cycle

intermediates, Fumarate, Succinate, and α-KG regulate Proline hydroxylase activity. In paragangliomas, pheochromocytomas, and a subset of sporadic gastrointestinal stromal tumors, a loss of function in FH or SDH, and mutated IDH inhibit the Proline hydroxylase, down-regulating the degradation of HIF-1[13]. (b) Similarly, a loss of function in FH or SDH, and mutated IDH inhibit α-KG dependent dioxygenase activity (here, JHDM and TETs), resulting in DNA hypermethylation in renal cancer, paragangliomas, and pheochromocytomas[46]

1.2 Metabolomics

1.2.1. LC-MS based high through put Metabolomics

Metabolism profiling, Metabolomics, has been broadly used and increasingly recognized as a powerful technology that links genotype and phenotype. A major tool for studying cellular metabolism is mass-spectrometry, which enables high throughput detection and quantification of metabolites. In metabolomics, there are two complimentary methodologies: targeted and untargeted. Targeted metabolomics enables to obtain highly quantitative metabolite concentration measurements. Generally, when performing a targeted metabolic analysis, the known chemical properties of the investigated compounds can be used to fine tune the sample preparation steps and analytical approaches[47].

The Shlomi lab has recently set up an LC-MS system, utilizing hydrophilic interaction chromatography coupled to an Orbitrap mass-spectrometer (Thermo's QExactive). We established methods for the targeted detection of ~300 metabolites, via a library of standards, including acids, amino acids, fatty acids, nucleotides, sugars, and sugar phosphates, etc.

Coupling of MS to chromatography has been widely used due to a higher level of sensitivity and precision of MS than that of other detectors[48]. A mass spectrometer consists of three

major parts: ion source, mass analyzer, and detector. Recent progression in LC-MS based protein and peptide biochemistry is attributed to the development of the electrospray ion source by Fenn in the 1980s[49]. This new technique enables ionization of a continuous liquid stream[47]. He was awarded the Nobel Prize in 2002 for his work in Mass spectrometry, together with Koichi Tanaka who developed matrix-assisted laser desorption ionization[47]. Electrospray Ionization (ESI) is well suited to the high through put analysis of various Biological molecules, which are moderately-polar[47]. Considering that ESI is a relatively soft method and minimizing the in-source fragmentation of analytes, it is compatible especially for the identification or quantification of small molecules in metabolomics[50].

Although LC-MS is widely used for the both targeted and untargeted metabolomics, current technology still have several challenges to address as follows. Firstly, it is extremely difficult to achieve stable LC-MS measurements due to many variable factors, such as the cleanliness of the ion source, ion optics and the collision cell, ion suppression, ion source flow rates, collision cell pressure and the ultimate MS vacuum[48]. Internal standard is used to deal with this issue, tracking the baseline change, but it is not straightforward to decide appropriate quantity to administer according to the dynamic range of each metabolite's detection. Besides, due to the analytical limitation of current methods in sensitivity and resolution, sufficient amount of biomass are required for sample preparation. Contrary to amplifiable DNA and RNA, since metabolites cannot be amplified[51,52], they should be pooled for current LC-MS protocol.

It has been revealed by various studies that even exponentially growing isogenic populations of microorganisms have cell-to-cell heterogeneity at their gene expression and growth rate[53–56]. Besides, accumulating evidence claims that slow-growing subpopulation can be involved in persistence[57], antibiotic resistance[58] and chemoresistance in cancer[59–61]. Due to the significant impact of the heterogeneity issue on health and disease[52], it has drawn attention; the NIH has funded to support single-cell profiling research, initially with US$2 million for 60 groups in 2014[52]. To advance and expand the knowledge in the single-

cell-level research especially for Metabolomics, several innovative technologies have been recently suggested. Researchers have tried to lower the detection limits to deal with the inability to amplify or to tag small-molecule metabolites (e.g. extracting larger amount of metabolites from bigger cells, such as the giant neurons of Aplysia californica, which have diameters up to 500µm and can be handled under a microscope[62,63], Mass Spectrometry Imaging[64–67], fluorescence-based detection[68,69] and vibrational spectroscopy[70,70,71]). To capture rapid metabolic dynamics, complicated preparation protocols have been modified and improved (e.g. microfluidics[70,70,71], nanoscale devices[70,70,71], and capillary electrophoresis and capillary LC[12]). However, still the procedure mostly requires either specialized platform for specific cells or slow isolation inevitably harboring perturbation on biological system. Hence, the single-cell-level Metabolomics is yet a rapidly growing field of biology with much room for improvement.

1.2.2. Isotope Tracing

The rate of metabolic reactions and pathways in living cells, also referred to as metabolic flux, is not a directly measurable quantity. The most direct approach for quantifying intracellular metabolic flux is isotope tracing[72,73]. The method is based on feeding cells with isotopically labelled nutrients (e.g. with ^{13}C), measuring the isotopic labelling of intracellular metabolites via LC-MS based technology, and computationally inferring metabolic fluxes (Figure 2). A metabolite with n carbons has 2^n distinct labeling patterns called *isotopomers* (with each carbon either labelled or not). LC-MS cannot detect the abundance of distinct isotopomers in a biological sample, but measures the relative abundance of each metabolite pool having different number of labeled carbons (i.e. *mass-isotopomers*). Hence, LC-MS practically measures the sum of abundances of different isotopomers, having a certain number of labeled carbons. Metabolic Flux Analysis (MFA) is a computational technique that enables to interpret isotopic labeling data and estimate metabolic fluxes. Recently, MFA has become a central technique in studies of cancer cellular metabolism[74,75].

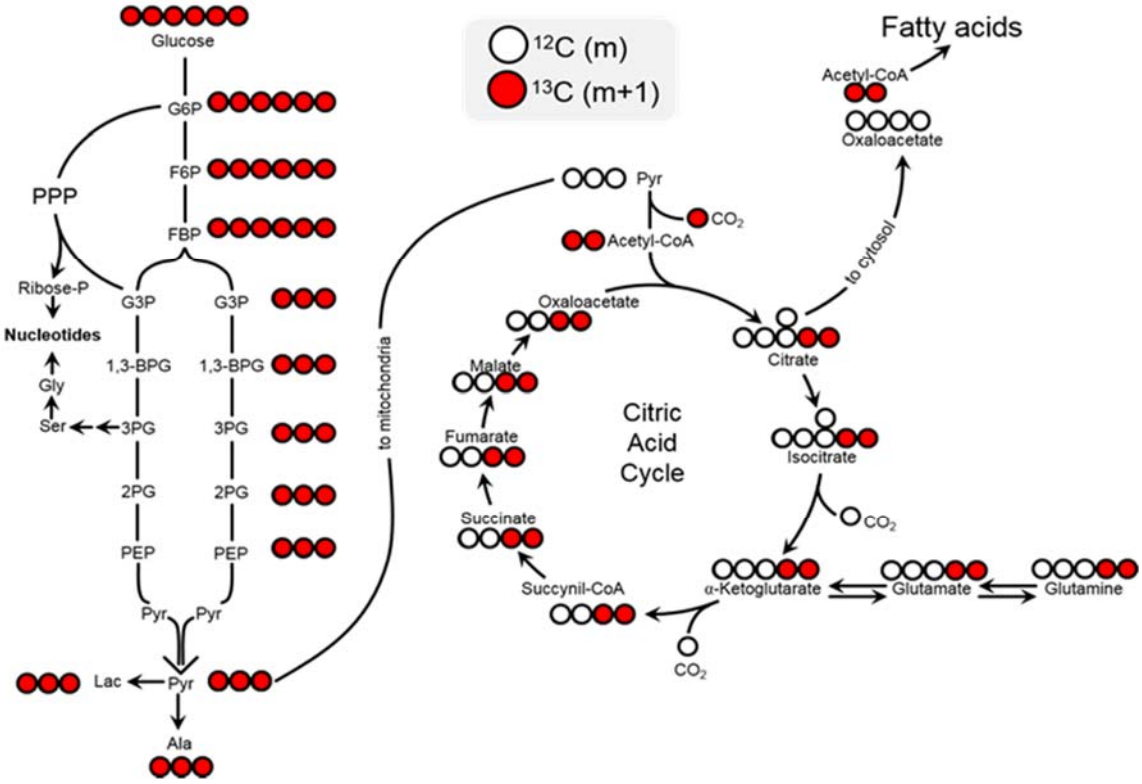

Figure 2: Feeding cells with [U-^{13}C] glucose labels glycolytic and TCA cycle intermediates. As shown, all glycolytic intermediates are fully labeled, while TCA cycle intermediates are only partially labeled, due to non-labelled carbons coming from media glutamine.

1.3. Metabolic flux analysis (MFA)

Fluxomics is the discipline that analyzes all fluxes in a cellular system[76]. To achieve fluxomics data, isotope tracing coupled with MFA is commonly used, and has recently become a central technique in studies of cancer cellular metabolism[74,75]. MFA studies were started from balancing fluxes around intracellular metabolites under the specific network stoichiometry assumption[77]. In this classical MFA method, empirical measurements such as nutrient uptake rate, growth rate, and CO_2 evolution rate are provided as constraints to

estimate intracellular fluxes. However, recently a large number of more advanced MFA techniques have been suggested and allow higher precision and reliability. To distinguish the characteristics of each MFA methods, we can determine major three criteria as following (Figure 3)[1]: (1) metabolic steady-state assumption, (2) labeling with stable-isotope tracers, and (3) isotopic steady-state assumption

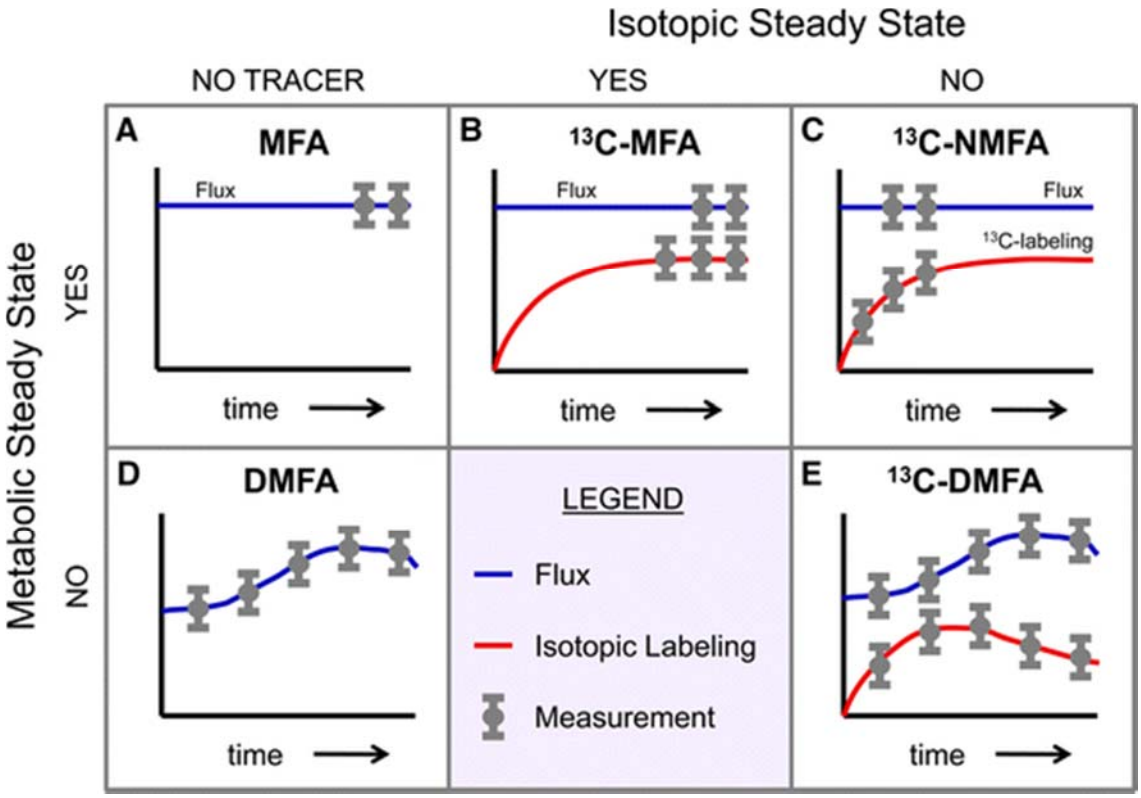

Figure 3: Classification of different methods for metabolic flux analysis[1] (figure from Antoniewicz, M. R. *J. Ind. Microbiol. Biotechnol.*, **42**, 2015). The major distinguishing criteria between metabolic flux analysis methods are whether stabled isotope tracer is applied, and whether metabolic (Isotopic) steady state is assumed. (A) MFA: (stochastic) Metabolic flux analysis, at metabolic steady state without isotopic tracers; (b) ^{13}C-MFA: ^{13}C-Metabolic flux analysis, at metabolic and isotopic steady state; (c) ^{13}C-NMFA: Isotopic non steady state ^{13}C-Metabolic flux analysis, at metabolic steady state and isotopic non-steady state; (d) DMFA:

Dynamic metabolic flux analysis, at metabolic non-steady state without isotopic tracers; and (e) ^{13}C-DMFA: ^{13}C-Dynamic metabolic flux analysis, at metabolic and isotopic non-steady state

In fact, applied to cell populations with cells at different phases of the cell cycle, classical MFA typically estimates the average flux throughout the cell cycle. Notably, performing isotope tracing experiments while not accounting for cell-cycle heterogeneity in a cell population may significantly bias the estimated population-level fluxes (Figure 4).

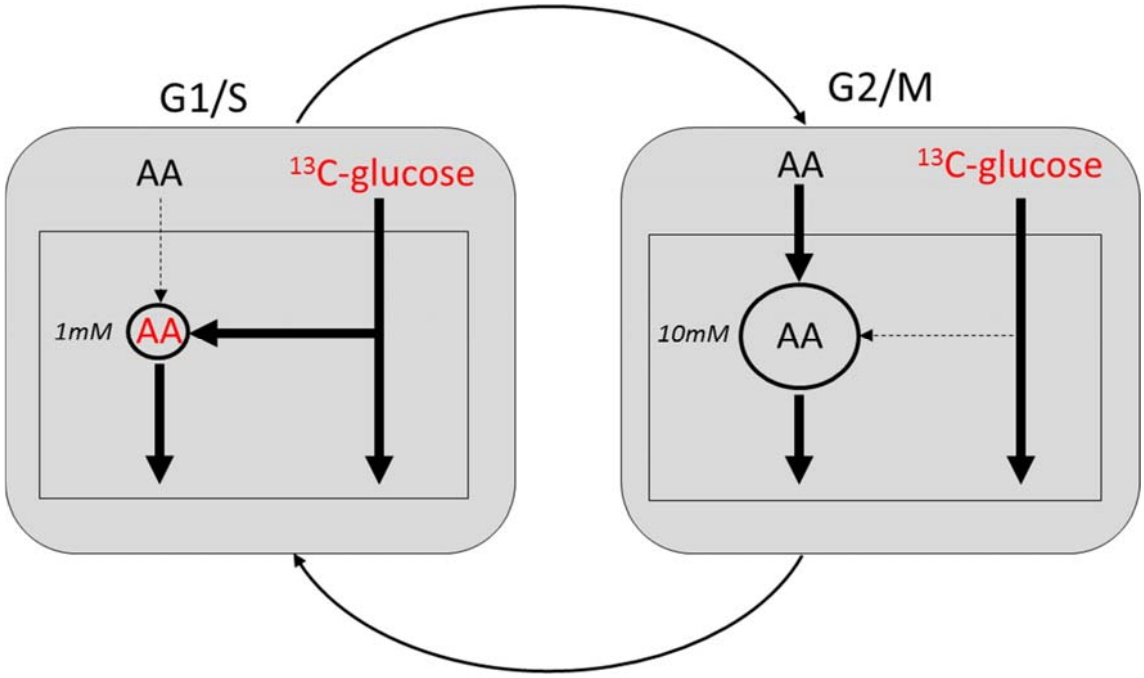

Figure 4: Existing isotope tracing techniques, not accounting for cell-cell variability may result in false estimation of "average" / population level flux. We consider the case where an amino acid (AA) is either de novo synthesized from glucose or taken up from the media. Assume that in G1/S, AA is being produced through de novo biosynthesis, resulting in AA being labelled when feeding ^{13}C-glucose; in G2/M, it is being mostly taken up from the media and hence does not get substantially labelled from ^{13}C-glucose. If the concentration of AA is substantially higher in G1/S in comparison to G2/M, and both G1/S and G2/M last for a roughly similar duration, AA will be mostly unlabeled in an unsynchronized cell

population (consisting of cells in both cell-cycle phases). This will lead standard MFA analysis to the false conclusion that AA is being mostly scavenged from media rather than de novo synthesized.

1.4. Metabolism and Cell cycle

Cell cycle progression is tightly interlinked with cellular metabolism [78]. The availability of sufficient metabolic nutrients and intracellular energy status control the ability of cells to enter and progress through cell cycle. The absence of glucose was first shown to arrest cells at the G1/S restriction point [79]. More recently, cellular energy status (ATP/AMP ratio) was found to regulate canonical cell cycle signaling pathways via AMP-activated protein kinase (AMPK) [80]. The mammalian target of rapamycin (mTOR) plays a central role in regulating cell cycle progression and growth, integrating stimuli of amino acid, energy, and oxygen availability [81,82]. Cell cycle progression is further controlled by intracellular metabolites affecting epigenetics: Nuclear acetyl-CoA levels, determined by nuclear ATP citrate lyase (ACL) [83], and pyruvate dehydrogenase (PDH) [84] regulate the acetylation of histones and thus control cell cycle progression [85,86]. Additionally, several metabolic enzymes were shown to directly regulate the cell cycle machinery, including PFKFB3 and PKM2, controlling the activity of cyclins and cyclin-dependent kinase (CDK) inhibitors in the nucleus [87–89].

Signaling pathways that coordinate cell cycle progression further regulate metabolic activity to support the changing metabolic demands throughout the cell cycle. The ubiquitin proteasome system, which tightly controls the concentration of cyclins, regulates the activity of two key enzymes in glucose and glutamine metabolism [90–92]; the ubiquitin ligase anaphase-promoting complex/cyclosome (APC/C) and ligase Skp1/cullin/F-box protein (SCF) complex control glycolytic flux via PFKFB3, restricting its expression to late G1 and early S; APC/C also regulates glutaminolysis via glutaminase 1 (GLS1), whose expression is induced in S and G2/M. Cyclins and cyclin-CDK complexes were further suggested to regulate central metabolic activities, including glycolysis, lipogenesis, and mitochondrial activity [93,94].

Furthermore, central oncogenes and tumor suppressors that control proliferation, growth, and cell cycle can stimulate the expression of enzymes that mediate glycolysis and glutaminolysis [95].

Overall, while the cell cycle machinery was found to regulate the concentration of key metabolic enzymes, an understanding of how the actual rate of metabolic reactions and pathway (i.e. metabolic flux) change throughout the cell cycle is still fundamentally missing.

1.5. Cell synchronization and Computational deconvolution

1.5.1. Cell synchronization strategy for mammalian cells

Synchronizing cell growth into specific cell cycle phases is an essential strategy in the cell cycle related research. The goal of a cell synchronization is collecting more homogeneous population under specific cell cycle to scrutinize the direct link between biological process and the focused cell cycle phases. There are several procedures that have proven effective in synchronizing mammalian cells into defined cell cycle phases.

Cell synchronization is achieved by either whole-culture synchronization methods or cell separation methods. The former uses the chemical inhibition of critical biological process in cell cycle progression, such as DNA replication or mitotic spindle formation, restricting cells to enter the next phase. Lovastatin (HMG-CoA retductase inhibitor)[96,97], and Mimosine (Ctf4/chromatic binding inhibitor)[98,99] mediates cell cycle arrest in early and late G1 phase, respectively. Feedback inhibition of DNA synthesis is induced by excess thymidine in media impede the progression in S phase[100]. Aphidicolin (DNA polymerase inhibitor), and Hydroxyurea (ribonucleotide inhibitor) prevent DNA replication and arrest cells in G1/S[101,102]. Inhibition of microtubule polymerization by Colchicine/colcemide or Nocodazole obstruct the progression in mitosis, synchronizing cells at G2/M phase[103–105]. Serum or Amino acid starvation have been also used to induce quiescence at G0/G1

phase[106–108]. Contact inhibition, or density-dependent inhibition enable normal cells to stop proliferation and arrest them at G1 phase though the inaction of transcriptional process[109,110].

Although most of cell separation methods are considered as less perturbative than whole-culture synchronization through any inhibition, in general specialized machinery is required for the procedures. Furthermore, subjected to metabolomics, large number of highly synchronized population is needed but not all the procedure suffice these requirements. For instance, flow cytometry and cell sorting is used for isolation of cells in specific stages based on the characterization of cells according to the fluorescence on antibody or dye or a rough measure for cell size by the scattered light intensity; however, flow cytometry based methods takes too long time to collect highly synchronized population[111]. Countercurrent centrifugal elutriation (CCE) is also capable of separating cells according to cell size[111]. Recently developed microfluidic “baby machine” for cell synchronization isolates newly born L1210 mouse lymphocytic leukemia cells using surface attachment chemistry[111]. Similarly, for adherent cells, mitotic shake-off (dislodgment of less adhesive mitotic cells) allows to isolate cells in mitosis[112,113].

1.5.2. Applying computational deconvolution for heterogeneous cell population and cell cycle research

Over the years, development of cell synchronization techniques has substantially contributed on studies about the metabolic changes involved in the cell cycle progression[78,114–117]. However, most of works ignore intra-cell cycle phase variability, assuming that the observed behavior of chemically or physically synchronized population can represent the character of a major subpopulation. This assumption may result in wrong analysis and misleading understanding. Furthermore, considering the cell cycle progression within a certain cycle phase, the cellular metabolism of the cells at the beginning and the

end of the same cell cycle phase might differ. Therefore, revealing the heterogeneity in synchronized cell populations is still a challenging, although a few studies have reported[2,118].

In the current LC-MS based Metabolomics platform, researchers typically extract pooled cell population from a LC-MS measurement. This is a pooled-average value, not more than a point estimate without containing any information about the distribution of cell populations. If there are cells in different cell cycle phases, considering only a pooled-average value may lead to incorrect result for the behavior of a subpopulation (Figure 5a and 5b). The measured LC-MS value may not represent the behavior of either one of all populations (Figure 5c). Furthermore, it is not feasible to find the relationship of two features (e.g., correlated or anti-correlated characteristics) from LC-MS measurements of two different metabolites without distribution information (Figure 5d).

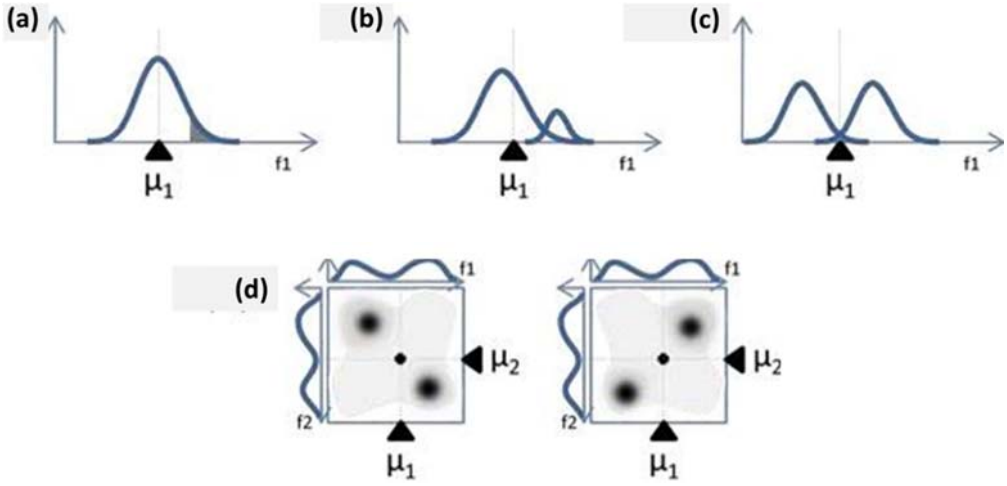

Figure 5: A point estimate, such as a pooled-average measurement, can mask the information about the distribution of subpopulations[2] (figure from Altschuler, S. J. & Wu, L. F. *Cell*, **141**, 2010). A pooled-average is referred as the μ_1 (μ_2) (a) A minor subpopulation is located at the tail of a distribution (shaded area) while the μ_1 is close to the mean of the major population; the μ_1 can be located at between the mean of the major and minor population. (b) The μ_1 is close to the mean of major population. (c) If there is a bimodal distribution, μ_1 is simply in the middle of two sub-populations. (d) If the population possess

multiple features, correlation relationship can be measured: correlated (left), and anti-correlated (right). However, based on a pair of point estimates, this information cannot be estimated.

An attractive solution is to extract specific data of cell cycle phase from heterogeneous samples via computational deconvolution techniques[119]. Computational deconvolution is the algorithm to find the function to reverse the effect of convolution from the raw data, providing information about the character of subpopulations. For example, the cell cycle phase information from FACS enables us to find the function to deconvolute the time-series omics data after synchronization.

In studies related to cell cycle specific gene expression, there have been few attempts to tackle this 'intra-cell cycle phase' heterogeneity by computational deconvolution to survey an association[3,119,120]. Due to the variance in cell-cell doubling time and any possible experimental artifacts during the synchronization procedure, the time-series data after synchronization exhibit a considerable variability. Therefore, time-series 'omics' data extracted after synchronization is always insufficient to predict the phenotype at the single-cell level. In the synchronization loss model, to deconvolute the expression data, each cell is assumed to progress through the cell cycle at the different intrinsic rate, following a Gaussian distribution[3] (Figure 6). The deconvolution algorithm aims to obtain the expected expression level from the perfectly synchronized population that can be achieved when all the cells enter and finish the same cell cycle phase together. Five parameters in this model were estimated based on empirical FACS measurements. For yeast cell cycle, considering the fact that budding or morphological changes are also other measures for cell cycle progression, a probabilistic model[120] and a branching process model[121] have been suggested for revealing the cell-cycle related transcription of yeast cells.

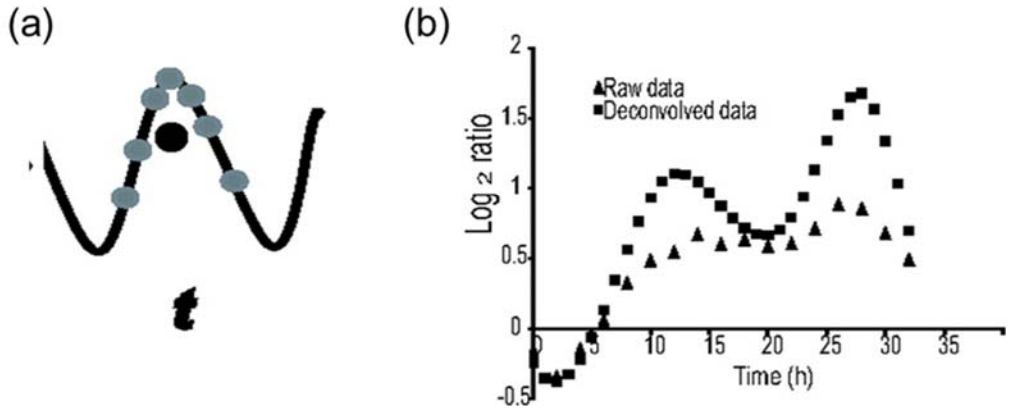

Figure 6: The data deconvolution by the synchronization loss model[3] (figure from Bar-Joseph, Z. et al. *Proc Natl Acad Sci U S A*, **105**, 2008). (a) Due to the loss of the synchrony after the synchronization, synchronized cells (gray dots) after time (t) from the release are distributed around the black dot, what we can measure from the time (t) sample. Using the synchronization loss model, the distribution of gray dots at time (t) can be determined. Using deconvolution on data from multiple time points, we can recover the underlying and deconvoluted time-series pattern (black line) of convoluted data. (b) Expression profile example of the BIRC5 gene after synchronizing cells with the thymidine block. Raw observed data (gray triangles) and deconvoluted data (black squares) by the synchronization loss model. When the underlying function is an oscillating wavelet, convoluted data typically lose the size of amplitudes. In other words, after computational deconvolution based on the synchronization loss model, deconvoluted data show larger amplitude than that of the observed raw data.

Research Aims and Significance

My research addressed the challenge of developing an integrated experimental-computational approach for analyzing metabolic flux changes throughout the cell cycle. Specifically, I addressed the following aims:

1. Develop a temporal-fluxomics ap**proach for quantifying metabolic oscillations throughout the cell-cycle**
    A. Establish an approach for isotope tracing through synchronized cell populations
    B. Computational deconvolution of metabolic measurements throughout the cell-cycle, facilitating inference of metabolic flux oscillations
2. **Determine how cells adapt their metabolism to fulfil the changing energetic and anabolic demands throughout the cell-cycle**
3. **Analyze how metabolic oscillations through the cell-cycle are regulated.**

2. Results

2.1. Cellular concentration of central metabolic intermediates oscillate throughout the cell cycle

To study metabolic dynamics throughout cell cycle, we synchronized HeLa cells using double thymidine block and applied high-throughput LC-MS based targeted metabolomics analysis to synchronized cell populations (> 10^6 cells per sample) in three-hour intervals for two complete cell cycles (see cell synchronization dynamics measured via propodium iodide staining/FACS analysis in Figure 7a; Figure 8; Methods). To obtain a reliable and accurate view of periodic metabolic oscillations and to overcome a potential perturbation of metabolism due to synchronization-induced growth arrest, we let synchronized cells complete one cell cycle before starting the LC-MS analysis (9 hours after cells are released in G1/S). Measured metabolite abundances in the synchronized cells were normalized by total cell volume in each time point to determine metabolite concentrations.

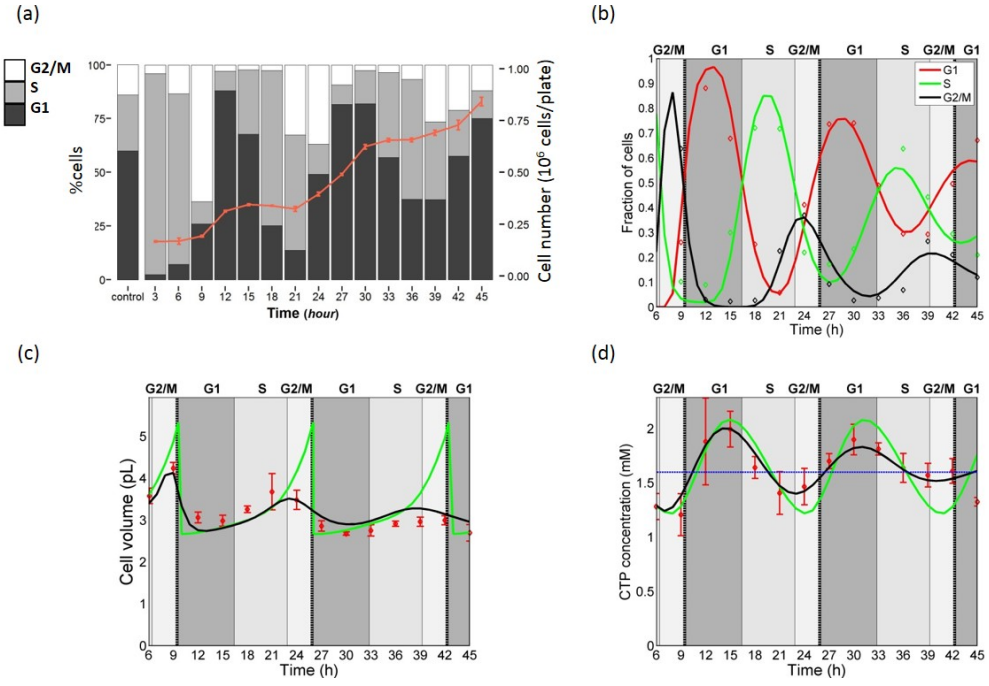

Figure 7: Detection of oscillations in metabolite concentrations throughout the cell cycle in HeLa cells revealed by LC-MS based metabolomics of synchronized HeLa cells and computational deconvolution. (a) Synchronization dynamics of a population of HeLa cells within almost 3 complete cell cycles measured via PI staining followed by FACS analysis. The increase in cell number following each mitosis is shown by an overlaid curve (in orange; mean and *s.d.* of *n=3*). (b) Computational modelling of the synchronization loss, considering 11% cell-cell variation in doubling time, shows that the simulated fraction of the cells in G1, S, and G2/M in the synchronized cells throughout the cell cycle (straight lines) match experimental measurements (marked with asterisk). (c) The measured average cell volume in the synchronized cell population (red; mean and *s.d.* of *n=3*; $v(t)$ in Equation 6), the deconvoluted signal (in case of no synchronization loss; green; $v'(x)$ in Equation 6), and the simulated average cell volume considering the loss in synchronization (black; matching the measured concentration data; Equation 6). (d) The measured concentration of CTP in synchronized cells shown in red (mean and *s.d.* of *n=5*; $u_i(t)$) in Equation 7; the deconvoluted concentration dynamics, in case of no synchronization loss (green; $u'(x)$ in Equation 7); and the expected concentration dynamics based on the deconvoluted concentrations and considering the loss in synchronization, matching the measured concentrations (black; Equation 7). The measured concentrations converge towards the steady-state concentrations measured in non-synchronized cells (horizontal blue line).

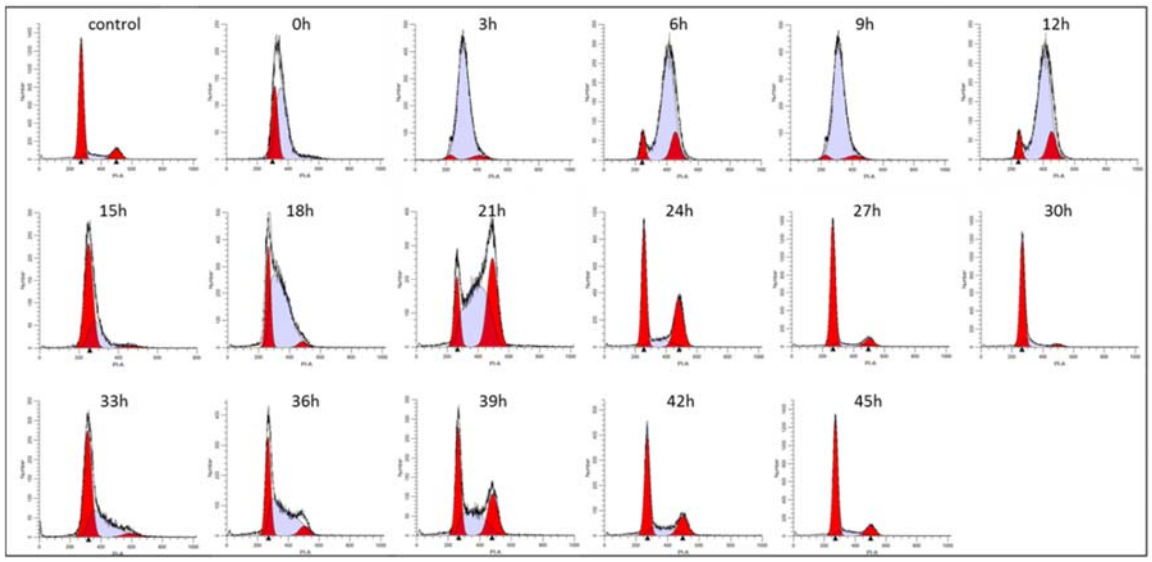

Figure 8: Measurement of cell cycle phase distribution in non-synchronized (control) and synchronized HeLa cells at different times after released from growth arrest, performed by propidium iodide (PI) staining/FACS analysis.

As cell synchronization is gradually lost with time due to inherent non-genetic cell-to-cell variability (a phenomenon also known as 'dispersion'), the distribution of cell cycle phases in the synchronized cell population becomes similar to that of non-synchronized cells after completing three rounds of replications (Figure 7a). To account for the loss of synchrony and to precisely quantify oscillations in metabolite levels, we employed "computational synchronization" [3]: We constructed a probabilistic model that describes the dynamics of the cell population loosing synchrony, assuming that each cell has its own "internal clock" which controls the cell cycle progression rate (see *synchronization loss model* in Methods*).* The parameters of the model were estimated by fitting a simulation of how the synchronized cell population progresses through the different phases of the cell cycle with corresponding FACS measurements, finding that cell-cell variability in the rate of cell cycle progression through the cell cycle is 11% (Figure 7b; Methods). We used this model for *computational deconvolution* of measured metabolomics data, estimating metabolite concentration

dynamics throughout the cell cycle, circumventing the impact of cell dispersion (Methods). Inferring the dynamics of metabolite concentrations throughout the cell cycle (rather than that of metabolite abundances) further required estimates of the dynamics of cell volume throughout the cell cycle. The latter was estimated based on deconvolution of total cell volume measurements performed in the synchronized cell population (Methods; Figure 3c). For example, the concentration of the nucleotide cytidine triphosphate (CTP) was found to oscillate throughout cell cycle, showing a ~50% increase in concentration in G1 phase versus G2/M phase (measured and deconvoluted concentrations shown in Figure 3d). As shown, the magnitude of the oscillation drops with time and converges to the steady state concentration measured in non-synchronized cells.

Our analysis reveals 57 metabolites whose concentrations significantly oscillate throughout the cell cycle (Figure 9; Dataset EV1; FDR corrected *p*-value < 0.05; Methods). Oscillations in nearly 44% of these metabolites could be detected only when in silico synchronization via computational deconvolution was applied (i.e. Equation 7 in Methods), emphasizing the strength of our pipeline. The median size of the observed oscillations is ~60% (difference between maximal and minimal concentration throughout the cell cycle); roughly one quarter of these metabolites show concentration changes larger than 2-fold throughout cell cycle. A significantly high fraction of the metabolites peak either in late G1 (~50% in the second half of G1; *p*-value < 10^{-5}; compared with the expected fraction assuming that concentration peaks are uniformly distributed throughout the entire cell cycle) or early S (~35% in the first half of S; *p*-value < 0.002).

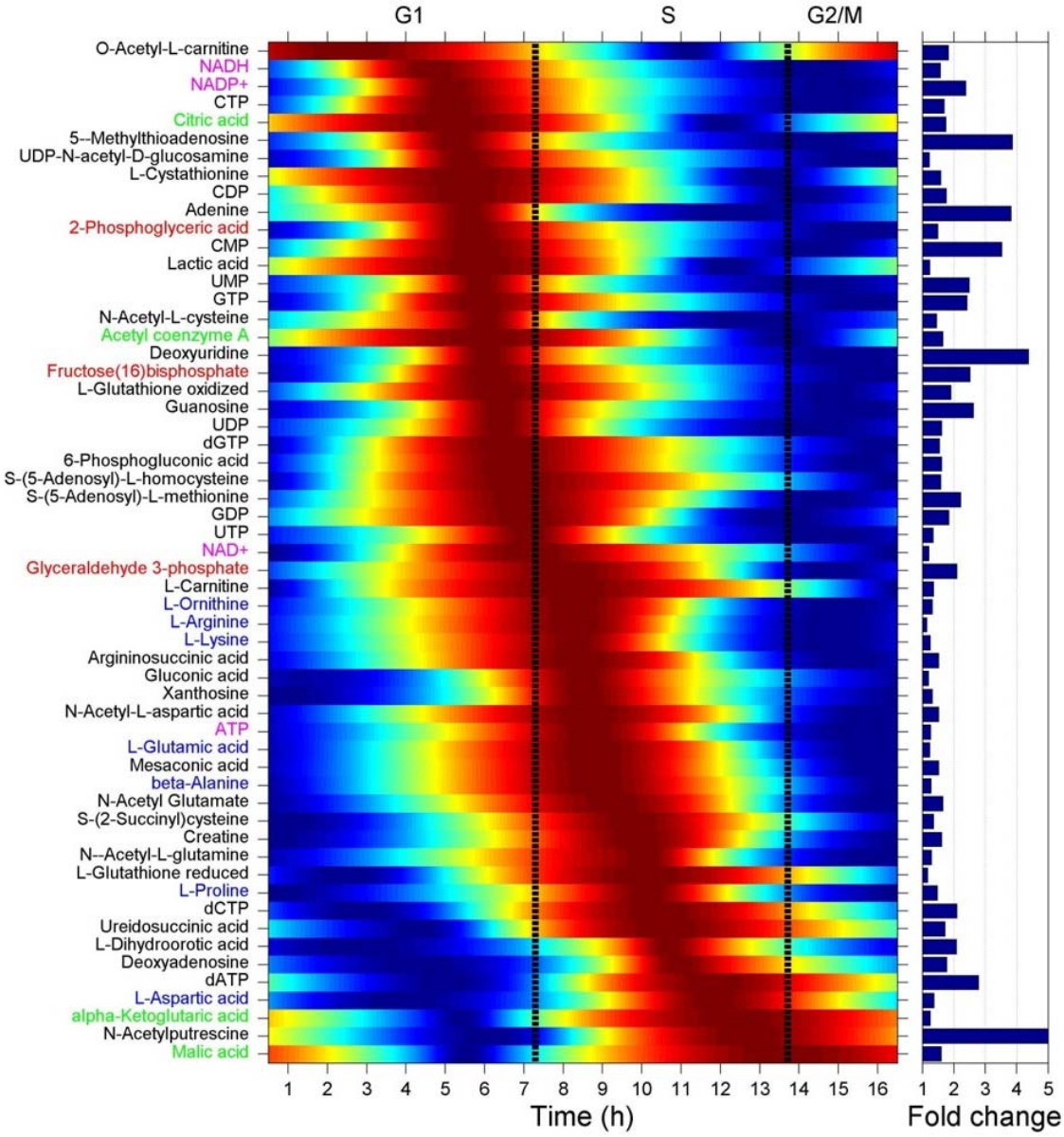

Figure 9: Oscillation in metabolite concentrations throughout the cell cycle in HeLa cells. The figure shows metabolites found to significantly oscillate throughout the cell cycle (concentrations normalized per metabolite; maximal concentration in red; minimal concentration in blue). The amplitude of the oscillations is shown on the right. Metabolites

are color-coded according to metabolic pathways: Energy/redox cofactors (purple); amino acids (blue); glycolytic metabolites (red); TCA cycle metabolites (green).

The oscillating metabolites include glycolytic and TCA cycle intermediates, nucleotides, amino acids, and energy and redox cofactors. Expectedly, the concentrations of the deoxynucleotides dCTP and dATP increase in S phase, when utilized for DNA replication. Intermediates in polyamine metabolism (5-methylthioadenosine, acetyl-putrescine, S-adenosyl-L-methionine, and S-adenosyl-L-homocysteine) show marked oscillations, in accordance with the known cell cycle dependent activity of this pathway [122]. Several glycolytic metabolites peak during G1/S transition, in accordance with reports of increased glycolytic flux at this cell cycle phase [91,115]. Cellular ATP/ADP ratio and redox potential (NADH/NAD+) further show a ~50% increase in the G1/S transition (Appendix Figure 10). Intracellular concentration of non-essential amino acids synthesized from consumed glutamine, including glutamate, ornithine, proline, and aspartate peak in S phase, in accordance with a reported increase in glutamine dependence in S phase [115,123]. Intriguingly, we find that different TCA cycle metabolites peak in distinct cell cycle phases: Acetyl-CoA and citrate peak in G1/S, while malic acid and α-ketoglutarate peak in late S, suggesting that the TCA cycle is rewired as cells progress through the cell cycle.

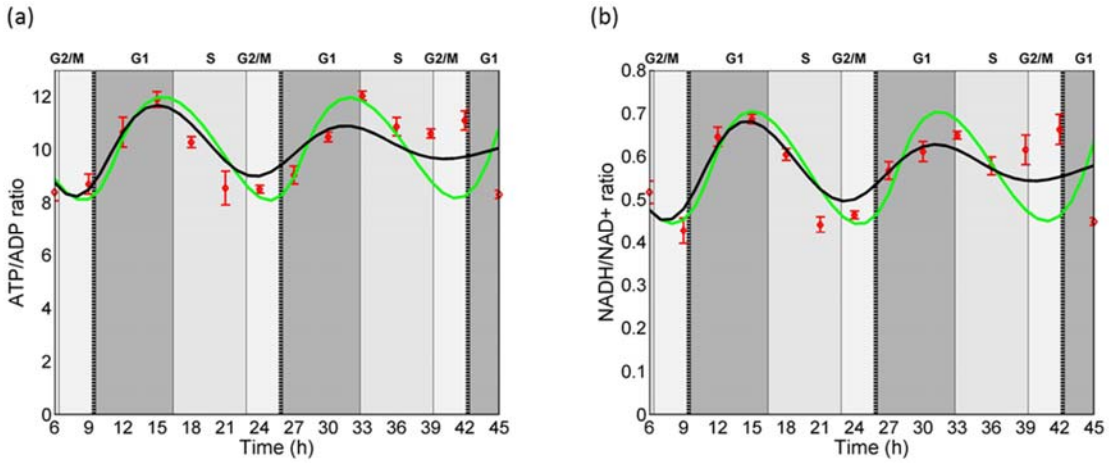

Figure 10: The measured and deconvoluted ATP/ADP ratio (a) and NADH/NAD+ ratio (b). Measured ratios in red (mean and *s.d.* of *n=5*); the deconvoluted signal (in case of no synchronization loss) in green; and the expected ratios considering the loss in synchronization in black.

3.2 Time-resolved fluxomics reveals increased glycolytic flux into TCA cycle in G1/S transition

To observe metabolic flux dynamics in TCA cycle and in branching pathways throughout the cell cycle, we performed pulse chase isotopic tracing experiments in synchronized HeLa cells with [U-^{13}C]-glucose and [U-^{13}C]-glutamine (one hour feeding), every three hours for two cell cycles (Figure 11a-b; Methods). Here, LC-MS was utilized to measure the mass-isotopomer distribution of metabolites (i.e. the fraction of each metabolite pool having zero, one, two, etc. labelled carbon atoms) after one hour of feeding with the isotopic tracers. Computational deconvolution was employed to analyze oscillations in metabolite isotopic labeling patterns while considering cell dispersion. The deconvolution approach is based on the observation that the measured fractional isotopic labeling of a metabolite in the synchronized cell population represents the average labeling in cells with distinct intrinsic times, weighted by the metabolite pool size in these cells (i.e. the measured isotopic labeling pattern is biased towards that of cells with an intrinsic time in which the metabolite pool size is larger than in others; Methods). Overall, we detected statistically significant oscillations in the isotopic labeling pattern of 21 metabolites when feeding isotopic glucose, and 16 metabolites when feeding isotopic glutamine (FDR corrected *p*-value < 0.05; Figure 11-12; Dataset EV2).

The inferred oscillations in metabolite isotopic labeling and concentrations were used to computationally analyze metabolic flux dynamics throughout the cell cycle, utilizing a variant of Kinetic Flux Profiling (KFP) [124] (Figure 12; in units of nmole/µL-cells/h; i.e., mM/h;

Methods). Specifically, given a metabolite whose isotopic labeling dynamics throughout the cell cycle was inferred as explained above, we search for the most likely transient production and consumption fluxes in each one-hour interval through the cell cycle, such that the simulated labeling kinetics of this metabolite (within the one-hour interval) would optimally match the experimental measurements (Methods; Figure 13-18). The simulation of the isotopic labeling kinetics of a metabolite of interest within a one-hour time interval is performed via an ordinary differential equations (ODE) model; relying on the inferred concentration of the metabolite within this time-interval (considering that a metabolite with a larger pool size would take more time to label, per unit of flux), as well as the isotopic labeling kinetics of intermediates that produce this metabolite. While KFP is typically applied to estimate fluxes under metabolic steady state (in which fluxes satisfy a stoichiometric mass-balance constraint), here, we constrain the difference between transient fluxes that produce and consume a certain metabolite according to the measured momentary change in the concentration of that metabolite.

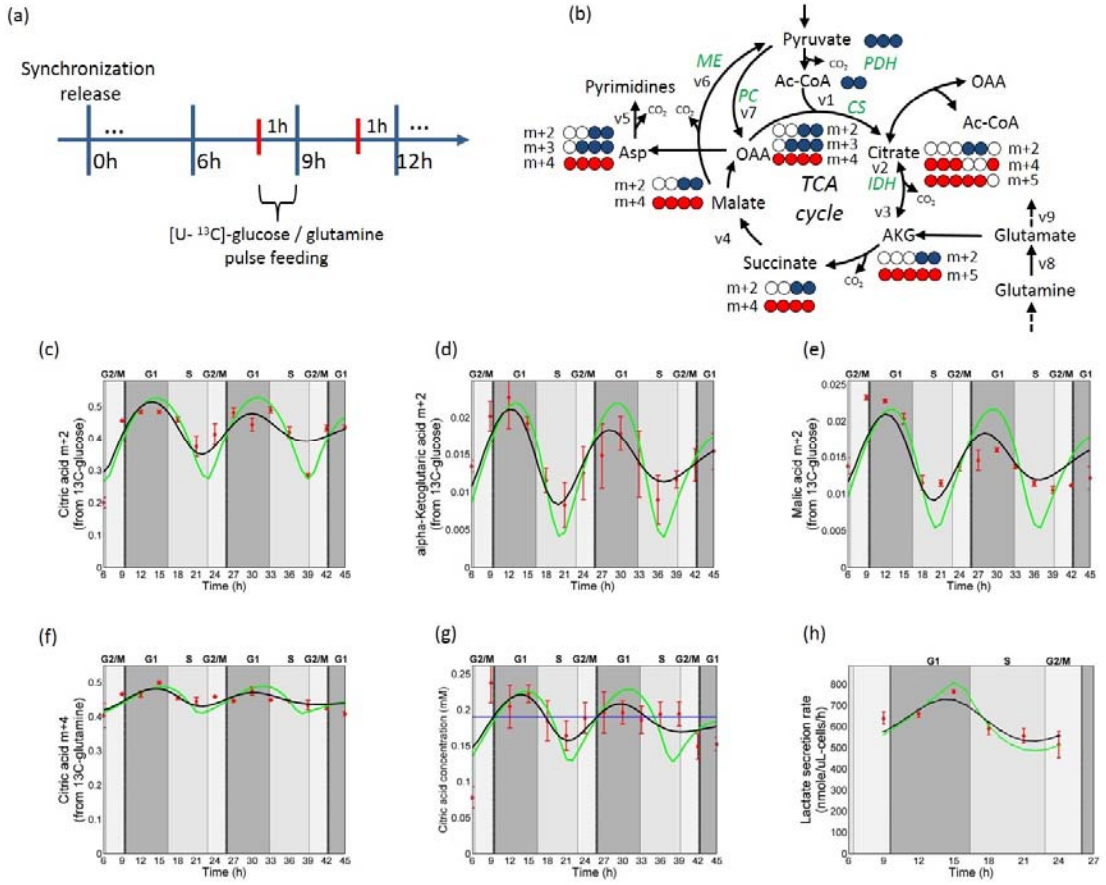

Figure 11: Oscillations in isotopic labeling of TCA cycle metabolites throughout the cell cycle from [U-^{13}C]-glucose show induced glycolytic flux into TCA cycle in G1/S. (a) Experimental scheme for a series of pulse-chase isotope tracing experiments in synchronized cells. (b) Atom tracing of TCA cycle metabolites from [U-^{13}C]-glucose (blue) and [U-^{13}C]-glutamine (red). (c-e) Measured relative fraction of the m+2 labeling of TCA cycle intermediates after feeding [U-^{13}C]-glucose (red; mean and *s.d.* of *n=3*), the deconvoluted signal (green), and the expected labeling dynamics considering the loss in synchronization (black; representing TCA cycle oxidation of glucose-derived acetyl-CoA). (f) Oscillations in citrate m+4 labeling after feeding [U-^{13}C]-glutamine (mean and *s.d.* of *n=3*). (g) Oscillations in the total citrate concentration throughout the cell cycle (mean and *s.d.* of *n=5*). (h) The measured lactate secretion flux in synchronized cells shown in red (mean and *s.d.* of *n=5*; $f_i(t)$ in Equation 9); the deconvoluted secretion flux dynamics, in case of no synchronization loss (green; $f_i'(x)$

in Equation 10); and the expected secretion flux based on the deconvoluted fluxes and considering the loss in synchronization, matching the measured fluxes (black; Equation 10).

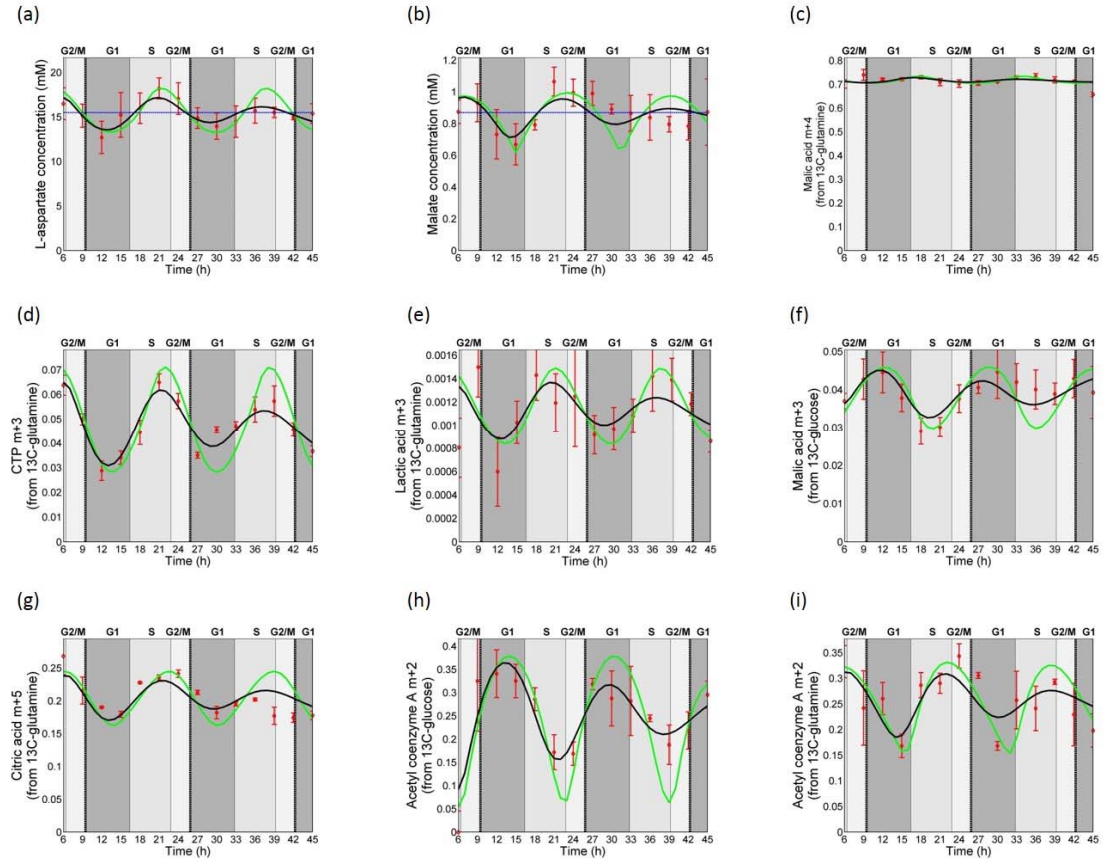

Figure 12: Oscillations in isotopic labeling of TCA cycle metabolites throughout the cell cycle from [U-^{13}C]-glutamine show induced oxidative and reductive glutamine metabolism in S phase. Oscillations in aspartate (a) and malate (b) concentrations throughout the cell cycle when feeding [U-^{13}C]-glutamine (representing oxidative TCA cycle activity). (c) Uniform malate m+4 labeling throughout the cell cycle (combined with the increase in malate concentration in S phase representing increased oxidative TCA cycle flux in S phase). (d) Oscillations in pyrimidines m+3 labeling throughout the cell cycle when feeding [U-^{13}C]-glutamine (representing de novo pyrimidine biosynthesis). (e) Oscillations in lactate m+3

labeling throughout the cell cycle when feeding [U-^{13}C]-glutamine (representing malic enzyme activity). (f) Oscillations in malate m+3 throughout the cell cycle when feeding [U-^{13}C]-glucose (representing pyruvate carboxylase activity). (g) Oscillations in citrate m+5 when feeding [U-^{13}C]-glutamine throughout the cell cycle (representing reductive IDH flux). (h) Oscillations in acetyl-CoA m+2 when feeding [U-^{13}C]-glucose, representing oxidative glucose metabolism. Oscillations in acetyl-CoA m+2 when feeding [U-^{13}C]-glutamine, representing reductive glutamine metabolism (i). For measurements of metabolite concentrations (a-b), red marks represent mean and *s.d.* of *n=5*. For measurements of fractional isotopic labeling (c-i), red marks represent mean and *s.d.* of *n=3*.

Oscillations in the isotopic labeling pattern of TCA cycle intermediates when feeding isotopic glucose suggest that glucose-derived flux into TCA cycle increases in G1 phase and then drops in S phase. The fractional labeling of the m+2 form of the TCA cycle intermediates citrate, α-ketoglutarate, and malate drops in S phase (Figure 11c-e). Feeding cells with isotopic glutamine, we further observed a drop in citrate m+4 produced from oxaloacetate via citrate synthase in S phase (Figure 11f). Combined with the drop in citrate concentration during S phase (Figure 11g), metabolic modelling reveals a ~2-fold decrease in glycolytic flux into TCA cycle as cells progress through S phase; citrate synthase flux drops from ~6mM/h in G1/S phase to ~3mM/h in late S phase (Figure 19a; Figure 13). TCA cycle oxidation of citrate via isocitrate dehydrogenase (IDH) shows similar flux dynamics, with ~2-fold drop in S phase (Figure 19c; Figure 14).

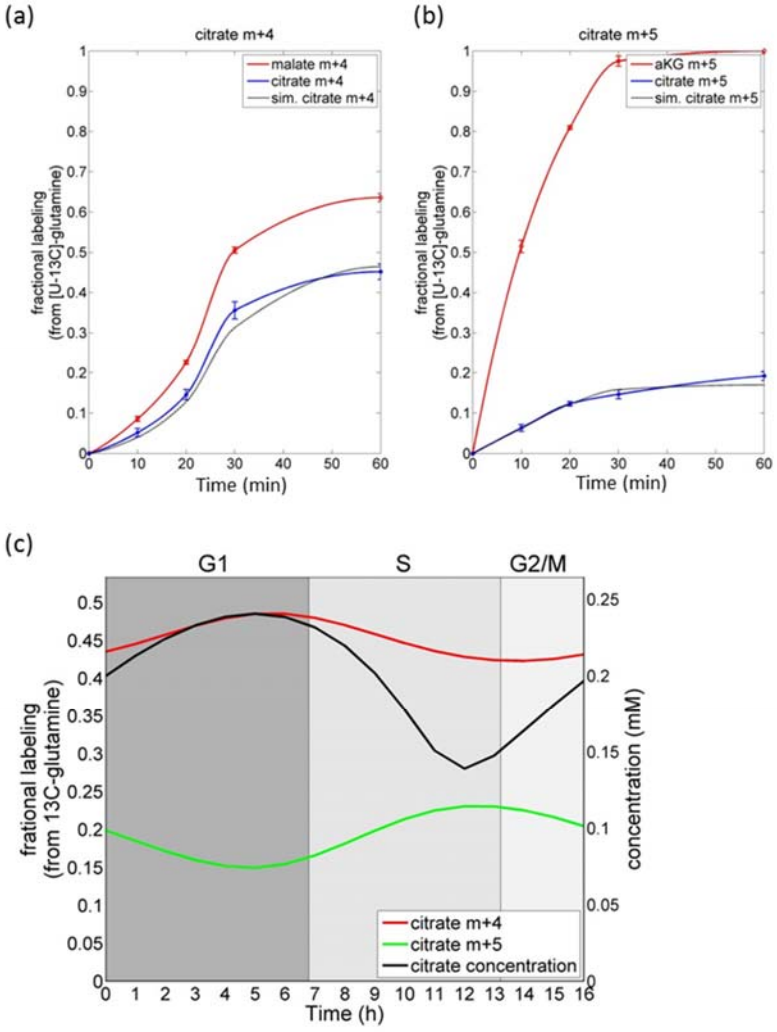

Figure 13: Computational modelling of citrate producing fluxes: Citrate synthase (*v1*) and reductive IDH (*v2*) fluxes. The measured (blue; mean and *s.d.* of *n=3*) and simulated (black curve) 1-hour labeling kinetics of citrate m+4 and m+5, as well as the measured labeling kinetics of malate m+4 (red; producing citrate m+4 via *v1*) and α-ketoglutarate m+5 (producing citrate m+5 via *v2*) in non-synchronized cells fed with [U-^{13}C]-glutamine (a-b). Estimating the flux through *v1* and *v2*, in non-synchronized cells, the simulated labeling kinetics of citrate m+4 and m+5 match the measured labeling kinetics. (c) The deconvoluted fractional labeling of citrate m+4 and m+5 after 1-hour feeding with [U-^{13}C]-glutamine and citrate concentration throughout the cell cycle.

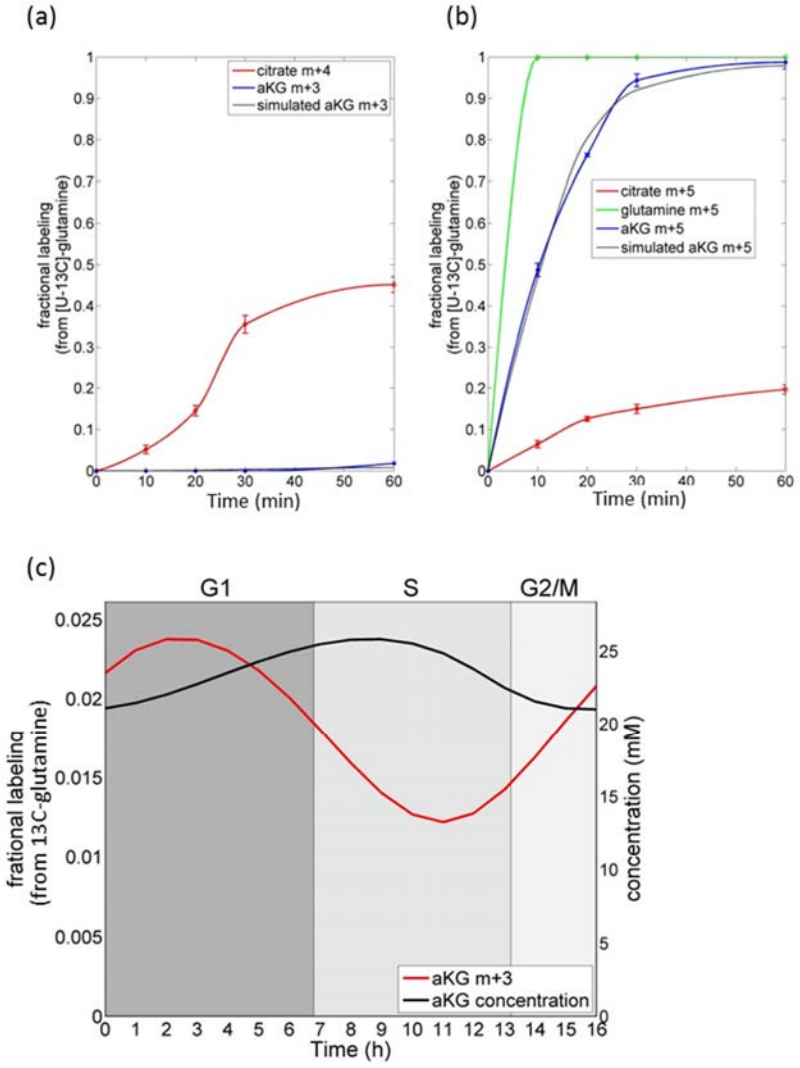

Figure 14: Computational modelling of fluxes producing α-ketoglutarate/glutamate: Glutamine->glutamate (v8) and oxidative IDH (v3) fluxes. The measured (blue; mean and *s.d.* of *n=3*) and simulated (black curve) 1-hour labeling kinetics of α-ketoglutarate m+3 and m+5, as well as the measured labeling kinetics of citrate m+4 (producing α-ketoglutarate m+3 via *v3*), citrate m+5 (producing α-ketoglutarate m+5 via *v3*), and glutamine (producing α-ketoglutarate m+5 via *v8*) in non-synchronized cells fed with [U-^{13}C]-glutamine (a-b). Estimating the flux through *v3* and *v8*, in non-synchronized cells, the simulated labeling kinetics of α-ketoglutarate m+3 and m+5 match the measured labeling kinetics. (c) The

deconvoluted fractional labeling of α-ketoglutarate m+3 after 1-hour feeding with [U-^{13}C]-glutamine and α-ketoglutarate concentration throughout the cell cycle.

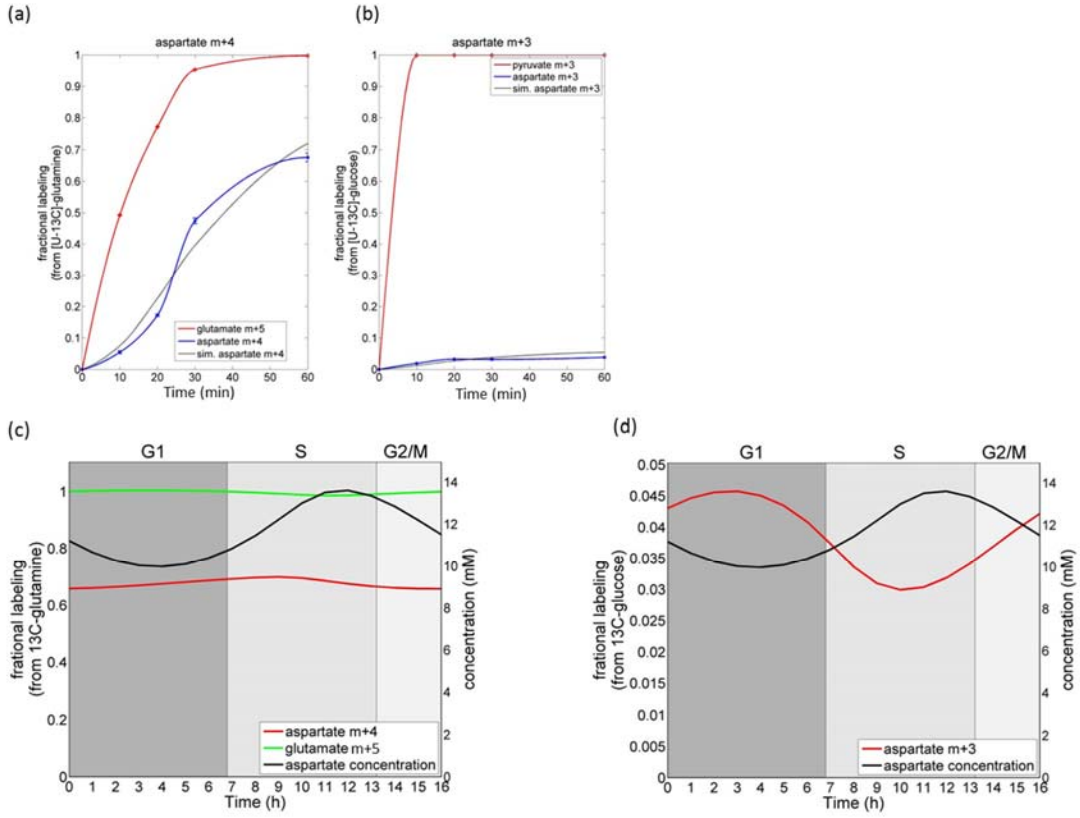

Figure 15: Computational modelling of malate/aspartate producing fluxes: α-ketoglutarate oxidation (*v4*) and pyruvate carboxylase (*v7*) fluxes. The measured (blue; mean and *s.d.* of *n=3*) and simulated (black curve) 1-hour labeling kinetics of aspartate m+4, and the isotopic labelling kinetics of glutamate m+5 (producing aspartate m+4 via *v4*), in non-synchronized cells fed with [U-^{13}C]-glutamine. (b) The measured (blue; mean and *s.d.* of *n=3*) and simulated (black curve) 1-hour labeling kinetics of aspartate m+3, and the isotopic labelling kinetics of pyruvate m+3 (producing aspartate m+3 via *v7*), in non-synchronized cells fed with [U-^{13}C]-glucose. (c) The deconvoluted fractional labeling of aspartate m+4 and glutamate m+5 after 1-hour feeding with [U-^{13}C]-glutamine, and

aspartate concentration throughout the cell cycle. (d) The deconvoluted fractional labeling of aspartate m+3 after 1-hour feeding with [U-^{13}C]-glucose and aspartate concentration throughout the cell cycle.

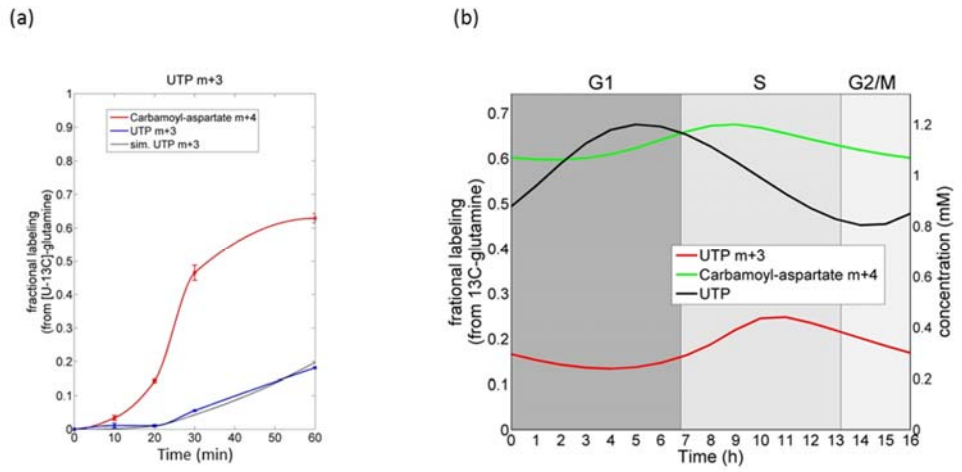

Figure 16: Computational modelling of the UTP producing flux (*v5*). (a) The measured (blue; mean and *s.d.* of *n=3*) and simulated (black curve) 1-hour labeling kinetics of UTP m+3 and measured labeling kinetics of carbamoyl-aspartate m+4 (producing UTP m+3 via *v5*), in non-synchronized cells fed with [U-^{13}C]-glutamine. Estimating the flux through v5 in non-synchronized cells, the simulated labeling kinetics of UTP m+3 matches the measured labeling kinetics. (b) The deconvoluted fractional labeling of UTP m+3 and carbamoyl-aspartate m+4 after 1-hour feeding with [U-^{13}C]-glutamine and UTP concentration throughout the cell cycle.

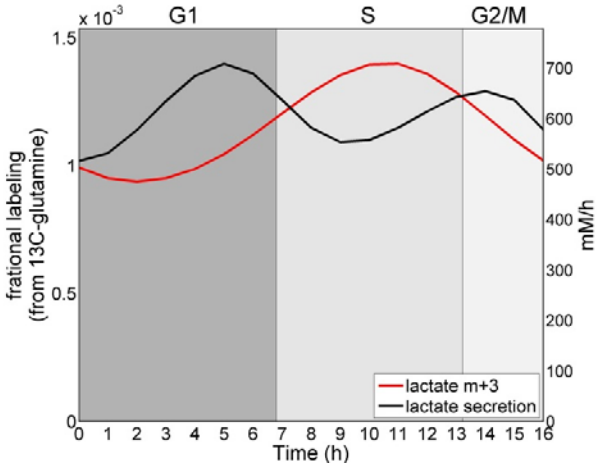

Figure 17: Computational modelling of malic enzyme flux (*v6*). The deconvoluted fractional labeling of lactate m+3 after 1-hour feeding with [U-^{13}C]-glutamine throughout the cell cycle (red); and lactate secretion flux throughout cell cycle (black).

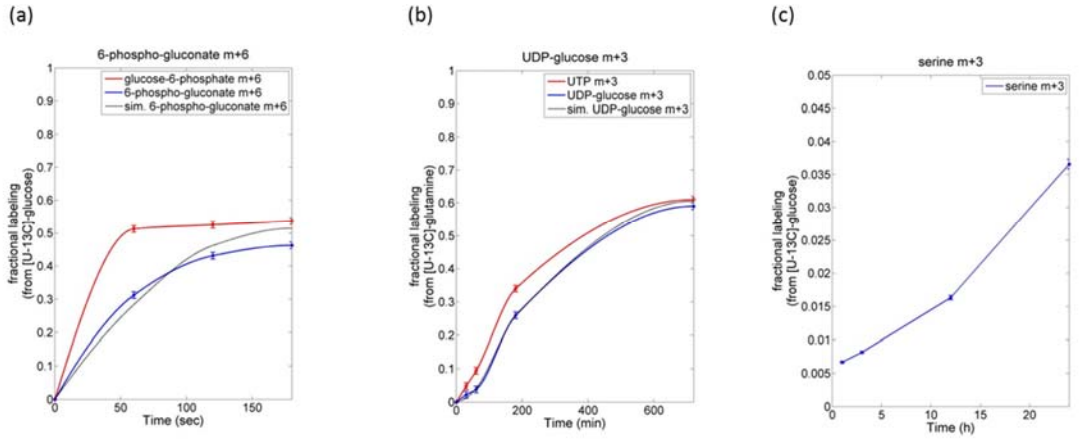

Figure 18: Quantifying metabolic flux through pathways branching out of glycolysis in non-synchronized cells. (a) Oxidative PPP flux is estimated based on the rate of labeling of 6-phospho-gluconate from glucose-6-phosphate, when feeding isotopic glucose (considering a 6-phospho-gluconate concentration of 0.04mM). Reductive PPP flux is roughly similar to oxidative PPP considering that the steady state m+1 labeling of ribose converges to ~50% when feeding [1,2-^{13}C]-glucose (not shown). (b) Glycogenesis flux is estimated based on the

rate of labeling of UDP-glucose m+3 from UTP m+3, when feeding isotopic glutamine (considering a UDP-glucose concentration of 0.26mM). (c) The fractional labeling of serine m+3 is less than 5% after feeding isotopic glucose for 24h; hence *de novo* serine biosynthesis is less than 5% of the total serine consumption rate from media (<10mM/h).

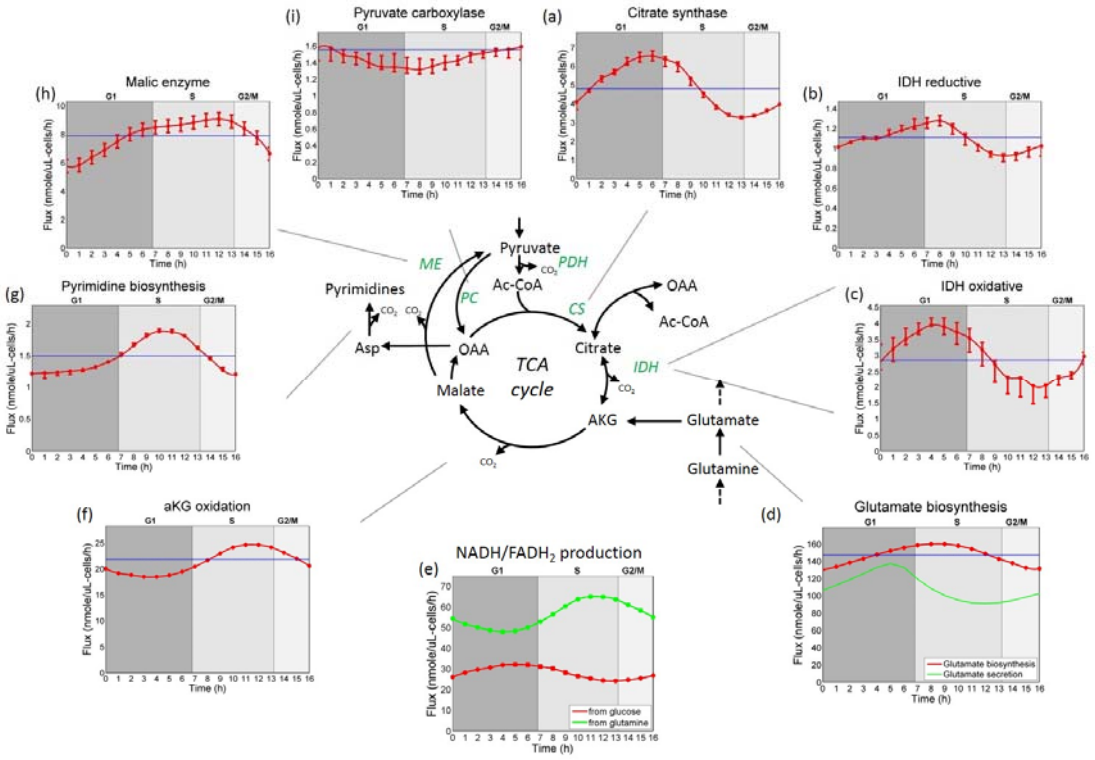

Figure 19: Complementary oscillations of glucose versus glutamine-derived fluxes in TCA cycle. (a-i) Oscillations in metabolic flux throughout the cell cycle (in mM/h), computed based on metabolic modelling of measured oscillations in metabolite concentrations and isotopic labeling (red and green marks represent optimal estimates of transient flux with 95% c.i.). Blue lines represent average fluxes inferred in a non-synchronized cell population. As shown, glucose-derived flux into TCA cycle peak in late G1 phase, while oxidative and reductive glutamine metabolism dominates S phase.

To examine whether the increase in glucose-derived flux into TCA cycle in G1/S is associated with increased in glycolytic flux, we measured lactate concentrations in the culture media in the synchronized cell population followed by computational deconvolution (Figure 11h; Methods). We find a ~65% increase in lactate secretion rate in G1/S transition. Considering that the average lactate secretion rate throughout the cell cycle is two orders of magnitude higher than that of pathways that branch out from glycolysis, the observed oscillation in lactate secretion represents cell cycle dependent changes in glycolytic flux: The average lactate secretion throughout the cell cycle is ~600mM/h, while oxidative pentose-phosphate pathway (PPP) is ~3mM/h, reductive PPP is ~3mM/h, glycogenesis is ~0.3mM/h, and serine biosynthesis is below 1mM/h (Figure 18). Overall, our data show that the increase in glycolytic flux in G1/S phase co-occurs with the increased glucose-driven flux entering the TCA cycle. Notably, analyzing oscillations in glycolytic flux based on direct measurement of changes in glucose consumption throughout the cell cycle (rather than based on lactate secretion) was not possible due to technical difficulty in accurately quantifying glucose consumption by synchronized cells within 3 hour time intervals (considering that the synchronized cell population consumes ~1% of the glucose in media within this short time period).

3.3 Induced oxidative and reductive glutamine metabolism compensates for the decreased glycolytic flux into TCA cycle in S phase

Glutamine feeds TCA cycle flux by producing glutamate, which is converted to α-ketoglutarate either via transamination or by glutamate dehydrogenase. As a first estimation of the cell cycle dynamics of glutamine-derived flux into the TCA cycle, we quantified cell cycle dependent glutamate production from glutamine versus glutamate secretion to the media. Tracing the m+5 labeling dynamics of glutamate when feeding [U-

^{13}C]-glutamine and glutamate concentration throughout the cell cycle suggest that glutamate production flux increases by 25% in S phase compared to G1 (Figure 19d). This is evident by a marked increase in glutamate concentration in S phase and similar m+5 glutamate labeling kinetics throughout the cell cycle (Figure 14). Glutamate secretion rate to the culture medium shows a marked drop in S phase, suggesting increased availability of glutamate for feeding the TCA cycle flux in S phase (Figure 19d). The increased entry of glutamine-derived flux into the TCA cycle in S phase is followed by a ~40% increase in α-ketoglutarate oxidation (Figure 19f; Figure 15). This is evident by the marked increase in malate and aspartate concentration in S phase (Figure 12a-b) and barely altered m+4 and m+3 labeling kinetics of these metabolites throughout the cell cycle, respectively (Figure 12c and 20).

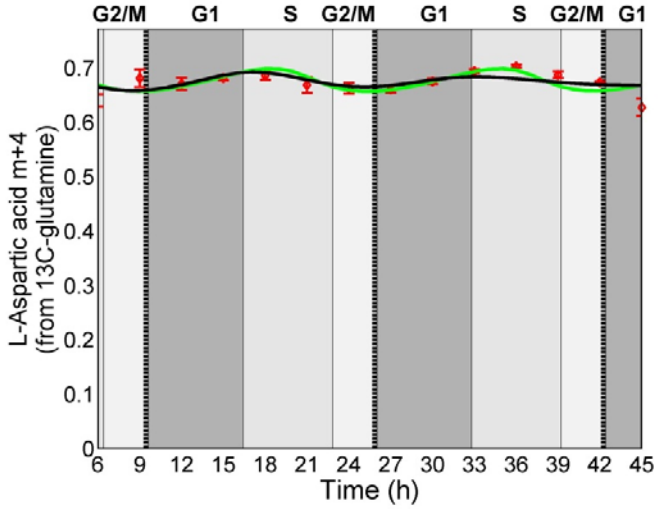

Figure 20: The cell cycle kinetics of L-aspartate m+4 when feeding synchronized HeLa cells with [U-^{13}C]-glutamine for one hour. Measured ratios in red (mean and *s.d.* of *n=3*); the deconvoluted signal (in case of no synchronization loss) in green; and the expected ratios considering the loss in synchronization in black.

The increased glutamine derived anaplerotic flux into the TCA cycle in S phase (via net production of the TCA cycle intermediate α-ketoglutarate) is balanced by oscillations in

cataplerotic fluxes, consuming TCA cycle intermediates for biosynthetic and bioenergetics purposes: We find a ~70% increase in pyrimidine biosynthesis flux in S phase, consuming oxaloacetate from TCA cycle (transaminated to produce aspartate; Figure 19g). This is evident by a marked increase in the m+3 labeling of pyrimidines in S phase (Figure 12d and 21), while considering the oscillations in the labeling kinetics of carbamoyl-aspartate in pyrimidine biosynthesis and pyrimidine concentrations (Figure 16). Oscillations in the biosynthetic flux of pyrimidines as well as purines is further supported by an increased m+5 labeling of pyrimidines and purines in S phase (i.e. having all five ribose carbons labelled) upon feeding with isotopic glucose (Dataset EV2). The malic enzyme flux (decarboxylating malate dehydrogenases) further shows a marked ~65% increase in S phase (Figure 19h; Figure 17), as evident by the increased lactate m+3 labeling in S phase when feeding isotopic glutamine (Figure 12e). Consistently, an increased concentration of lactate m+3 in the culture media is further observed in S phase (Figure 22). Notably, while glutamine-derived anaplerotic flux increases in S phase, there is no major change in glucose-derived anaplerotic flux through pyruvate carboxylase in S phase (Figure 19i; Figure 15). This is evident by the drop in malate and aspartate m+3 in S phase when feeding isotopic glucose (Figure 12f and 23) occurring while the concentration of malate and aspartate increase (Figure 12a-b).

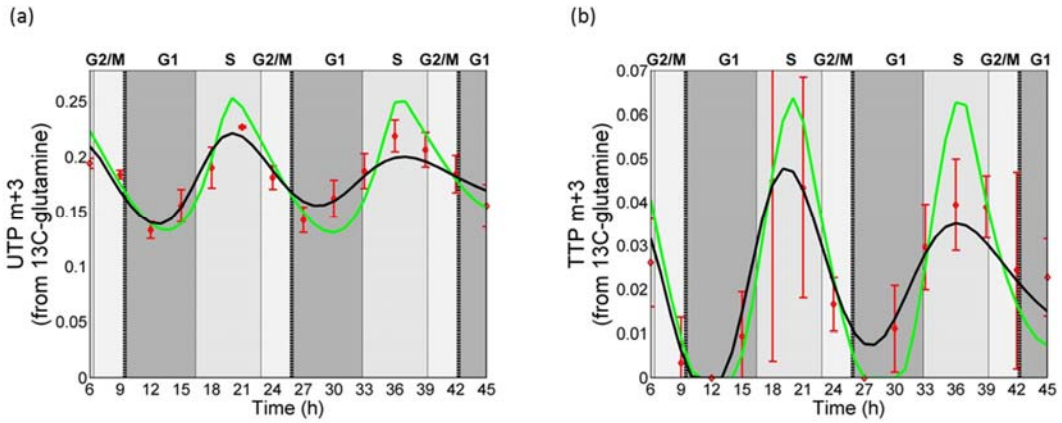

Figure 21: The cell cycle kinetics of UTP m+3 and TTP m+3 when feeding synchronized HeLa cells with [U-^{13}C]-glutamine for one hour. Measured ratios in red (mean and *s.d.* of *n=3*); the deconvoluted signal (in case of no synchronization loss) in green; and the expected ratios considering the loss in synchronization in black.

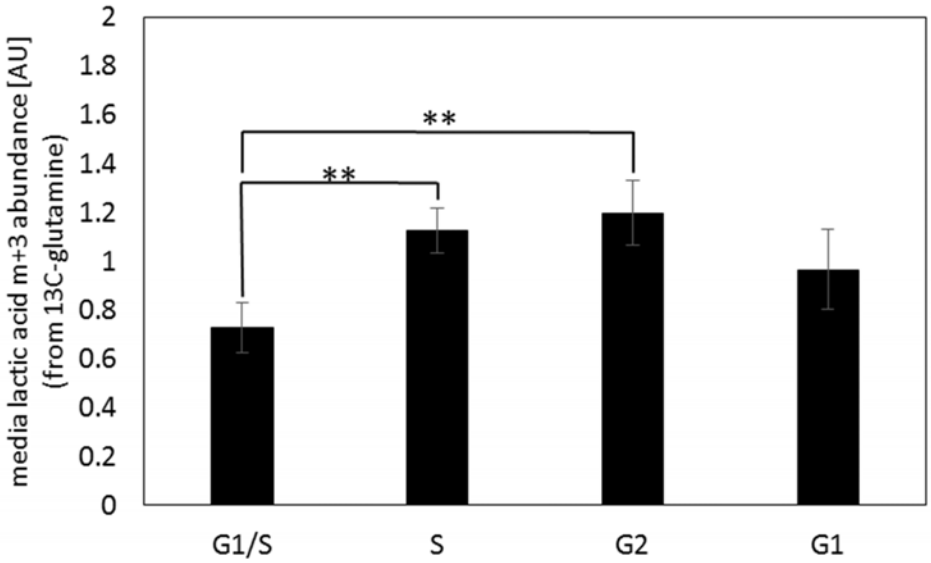

Figure 22: The measured abundance of lactate m+3 in media samples when feeding synchronized cells with [U-^{13}C]-glutamine for three hours. ** indicates *p-value* from Student's t-test ≤ 0.01.

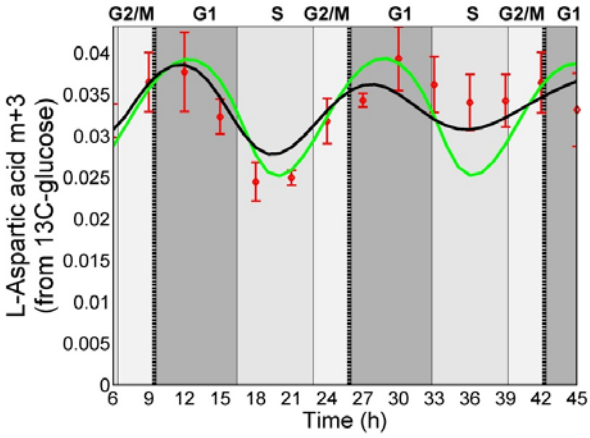

Figure 23: The cell cycle kinetics of L-aspartate m+3 when feeding synchronized HeLa cells with [U-^{13}C]-glucose for one hour. Measured ratios in red (mean and *s.d.* of *n=3*); the deconvoluted signal (in case of no synchronization loss) in green; and the expected ratios considering the loss in synchronization in black.

While the increased glutamine-derived flux into the TCA cycle in S phase supports an increase in α-ketoglutarate oxidation, we further detect a surprisingly high ~55% increase in the rate of α-ketoglutarate reduction in early S phase (Figure 19b; Figure 13). This is evident by the marked increase in m+5 citrate in S phase when feeding isotopic glutamine (Figure 12g). Considering the major drop in glycolytic flux into the TCA cycle in S phase, the relative contribution of reductive IDH to citrate production increases from ~15% in G1 to ~24% in S phase. Cell cycle oscillations in the relative contribution of glucose versus glutamine to citrate biosynthesis are further observed in the labeling of acetyl-CoA (produced in cytosol from citrate via ATP citrate lyase), where the fractional labeling of acetyl-CoA m+2 from [U-^{13}C]-glucose peak in G1 phase (Figure 12h) and acetyl-CoA m+2 from [U-^{13}C]- glutamine in S phase (Figure 12i). Accordingly, acetylated amino acids show increased m+2 labeling from glucose in G1 and from glutamine in S phase (Figure 24).

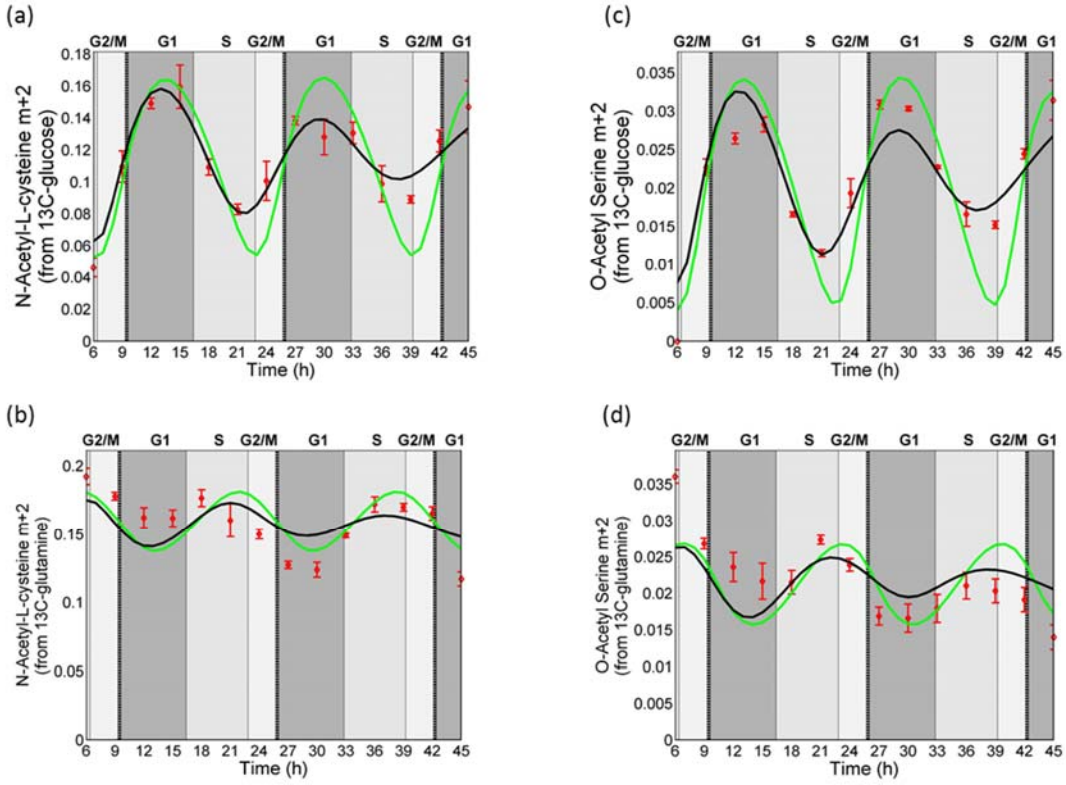

Figure 24: Oscillations in m+2 labeling of N-acetyl-cysteine (a-b) and O-acetyl-serine (c-d) when feeding isotopic glucose (a and c) and isotopic glutamine (b and d). Measured ratios in red (mean and *s.d.* of *n=3*); the deconvoluted signal (in case of no synchronization loss) in green; and the expected ratios considering the loss in synchronization in black.

The complementary oscillations in glucose versus glutamine derived flux into the TCA cycle result in an overall uniform production rate of reducing equivalents ($NADH/FADH_2$) ~85±5mM/h throughout the cell cycle (Figure 19e; Methods): Glucose-derived production of reducing equivalents peaks in G1/S while glutamine-derived production of reducing equivalents peaks in late S phase. While the relative contribution of glutamine to $NADH/FADH_2$ production oscillates (between ~60% in G1/S and ~75% in late S phase), it remains the prime source of reducing power for driving oxidative phosphorylation all throughout the cell cycle, in accordance with previous measurements in non-synchronized

cells [125]. Consistent with the total production rate of NADH/$FADH_2$ remaining constant throughout the cell cycle, we find that oxygen consumption rate does not change throughout the cell cycle (Figure 25). Hence, the complementary oscillations in glucose versus glutamine oxidation in TCA cycle result in a constant rate of reducing equivalent production, sustaining a constant rate of mitochondrial oxidative phosphorylation flux throughout the cell cycle.

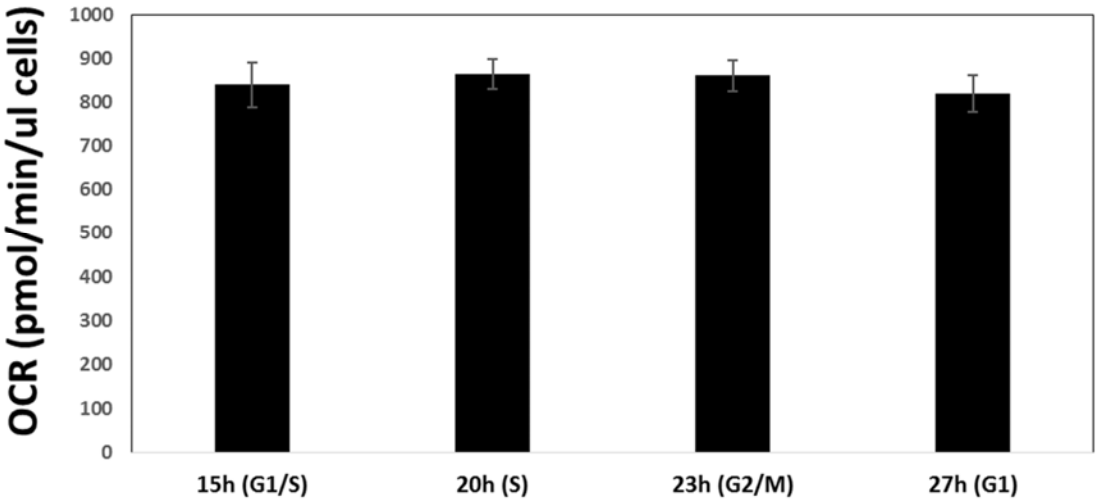

Figure 25: Oxygen consumption used for oxidative phosphorylation in synchronized HeLa cells, measured using a Seahorse XFp Flux Analyzer (the non-mitochondrial oxygen consumption after treatment with the ETC inhibitors rotenone and antimycin A subtracted from the basal OCR). No significant differences were found in the rate of oxygen consumption in different cell cycle phase. Data have been represented in averages ± SD from *n=3* replicates).

3.4 Suppression of glycolytic flux into TCA cycle in S phase is important for cellular progression through the cell cycle

The drop in glycolytic flux into TCA cycle in S phase (Figure 19a) involves a major two-fold decrease in flux through pyruvate dehydrogenase (PDH), the prime source for acetyl groups for TCA cycle oxidation. PDH is negatively regulated by pyruvate-dehydrogenase kinase (PDK) and treatment with the PDK inhibitor dichloroacetate (DCA) was previously shown to enhance glycolytic flux into TCA cycle while decreasing reductive glutamine metabolism towards citrate biosynthesis [126]. Accordingly, treating the synchronized HeLa cells with 4mM of DCA for one hour leads to a marked increase in the fractional labeling of citrate m+2 and acetyl-CoA m+2 from isotopic glucose, representing a major increase of glycolytic flux into the TCA cycle (Figure 26a-b). Notably, DCA treatment completely eliminates the oscillations in glycolytic flux into the TCA cycle, as evident by a uniform fractional labeling of citrate m+2 and acetyl-CoA m+2 when feeding DCA throughout the cell cycle. DCA treatment further leads to a uniform citrate m+5/m+4 ratio and fractional labeling of acetyl-CoA m+2 from isotopic glutamine, eliminating the oscillations in glucose versus glutamine flux towards acetyl-CoA production (Figure 26c-d).

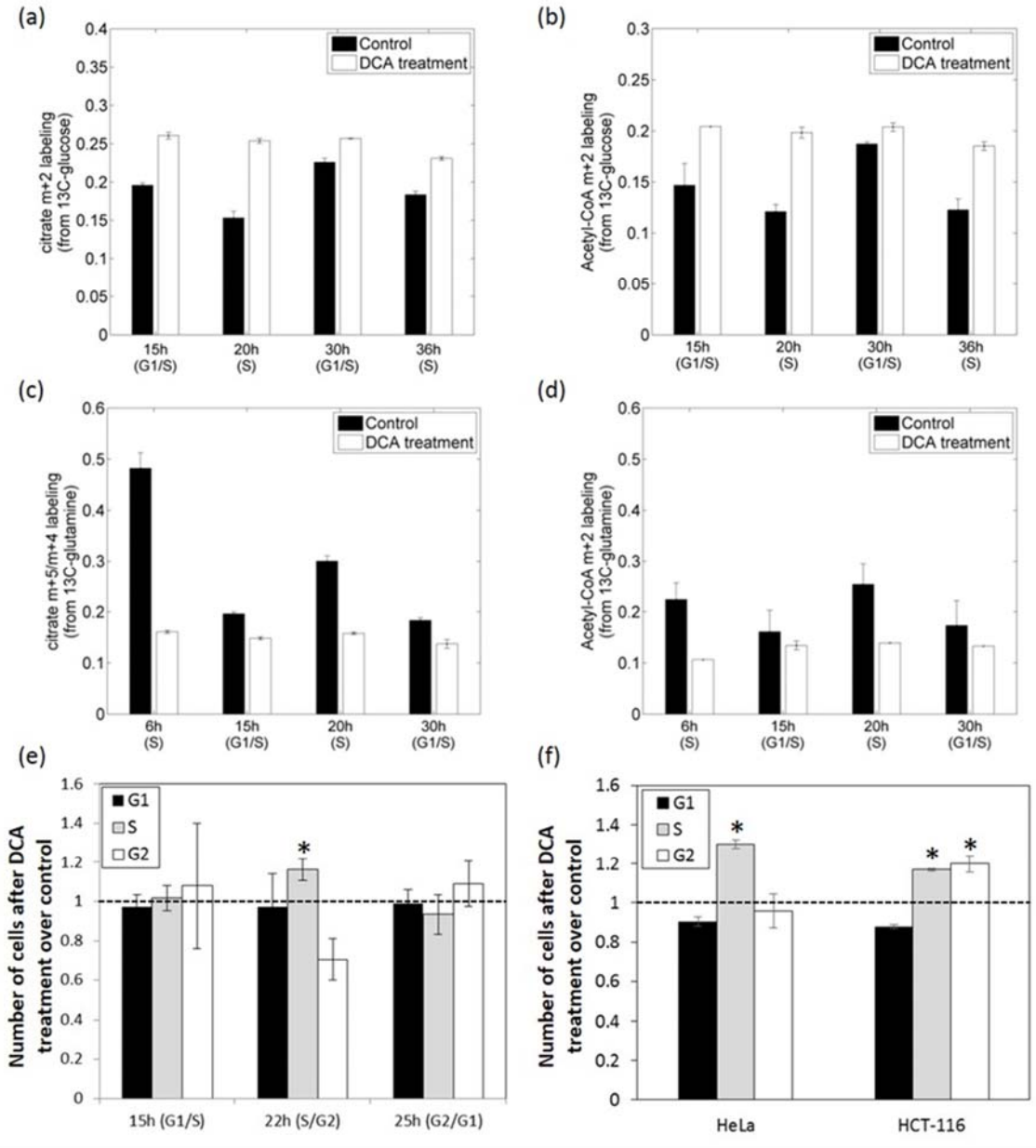

Figure 26: PDK inhibition via DCA treatment eliminates the oscillation of glycolytic flux into TCA cycle and inhibits cellular progression through S phase. (a-b) One hour treatment of synchronized cells with DCA inhibits the oscillations in citrate m+2 (a) and acetyl-CoA m+2 (b) from isotopic glucose (representing glycolytic flux into TCA cycle). It further inhibits oscillations in citrate m+5/m+4 ratio (c) and acetyl-CoA m+2 (d) from isotopic glutamine (representing oxidative versus reductive TCA cycle flux). (e) The fraction of cells in G1, S,

and G2/M phases in synchronized HeLa cells after 3 hour treatment with DCA (normalized by measurements in untreated control cells). (f) The fraction of cells in G1, S, and G2/M phases in non-synchronized HeLa and HCT-116 cells after 24 hour treatment with DCA (normalized by measurements in untreated control cells). As shown, DCA significantly increases the fraction of cells in S phase, inhibiting cellular progression into G2 phase; showing mean and *s.d.* of *n=3* for all isotopic labeling forms and FACS measurements (a-f). Statistical significance of changes in the fraction of cells in each cell cycle phase following DCA treatment is calculated based on two-tailed, unequal variance t-test (e-f).

To test whether the suppression of glycolytic flux into TCA cycle in S phase is important for progression of cells through the cell cycle, we measured the cell cycle phase distribution in synchronized HeLa cells after three hour treatment with DCA. We find that DCA treatment leads to 16% increase in the fraction of cells in S phase (Figure 26e; two-tailed t-test *p*-value = 0.006). Treating of non-synchronized HeLa cells as well as colon carcinoma cells (HCT116) with DCA for 24 hours further shows a significant increase in the fraction of cells in S phase (Figure 26f; 30% increase in HeLa, two-tailed t-test p-value<10^{-3}; 17% increase in HCT116, p-value<10^{-5}). Notably, the observed increase in the fraction of cells in S phase represents slower progression rate of cells through S phase rather than cell cycle arrest at that phase, as almost all HeLa cells (~97%) complete at least one cell cycle after a 72 hour treatment with DCA (Figure 27). Conversely, treating of cells with a mitochondrial pyruvate carrier inhibitor (UK5099), which slows glycolytic flux into TCA cycle, shows the opposite effect of lowering the fraction of cells in S phase (Figure 28). Overall, our results indicate that the shift from glucose to glutamine-derived flux into TCA cycle plays an important role in cellular progression through S phase.

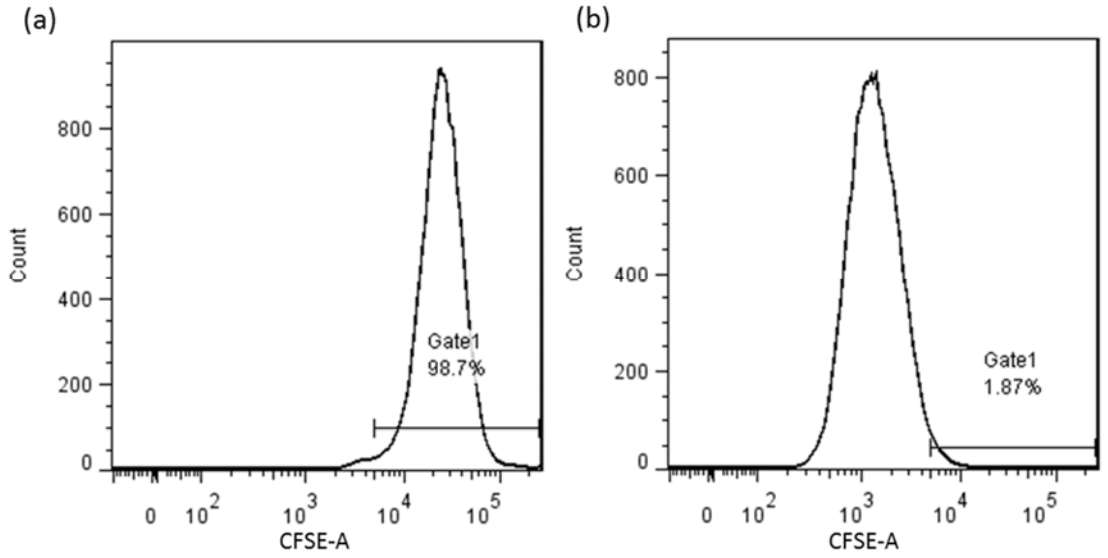

Figure 27: FACS measurement of CFSE signal in non-synchronized HeLa cells immediately after feeding to cells (a) and after 72 hours (b).

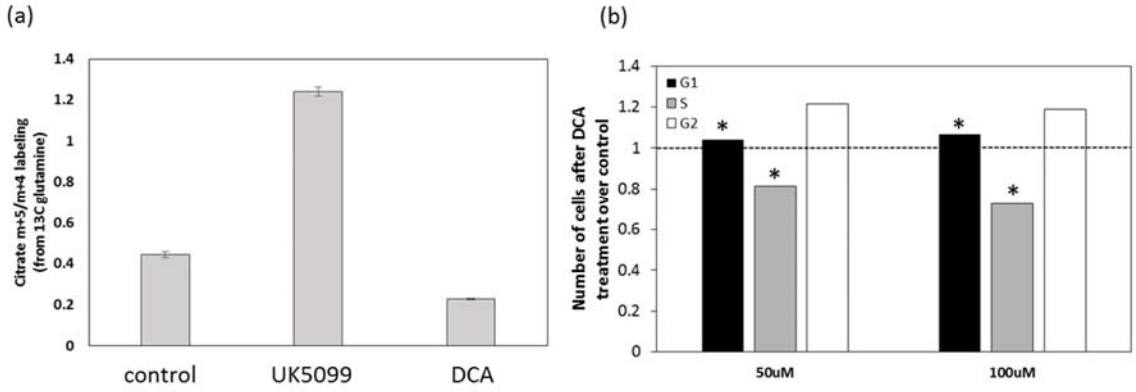

Figure 28: The mitochondrial pyruvate transporter inhibitor (UK5099) decreases oxidative TCA cycle flux and the fraction of cells in S phase. (a) Citrate m+5/m+4 ratio when feeding non-synchronized HeLa cells with an inhibitor of the mitochondrial pyruvate transporter (UK5099) and when feeding DCA. (b) The fraction of cells in G1, S, and G2/M phases in non-synchronized HeLa cells after 24 hour treatment with UK5099 (normalized by measurements in untreated control cells)

3. Discussion

We described a temporal-fluxomics approach for analyzing the dynamics of intracellular metabolic flux throughout the cell cycle in proliferating human cells. Inferring cell cycle dependent changes in flux is technically challenging due to several factors including the perturbative nature of synchronization-induced growth arrest, the gradual loss of population synchrony, and the requirement for accurate measurements of oscillations in metabolite pool sizes that in many cases vary by less than two-fold at maximum. Addressing these challenges, we tracked synchronized cells for three complete cell cycles, performed LC-MS based metabolomics and pulse-chase isotope tracing in the synchronized cells, and employed computational deconvolution techniques to reliably detect oscillations in metabolite concentrations and isotopic labelling dynamics. Inferring transient fluxes within each one hour interval throughout the cell cycle was complicated by the fact that the labelling of TCA cycle intermediates in the synchronized cells does not reach isotopic steady state within one hour feeding with the isotopic nutrients. This was addressed by modelling the isotopic labelling kinetics of metabolites within each one hour interval throughout the cell cycle; for each one time interval using an approach conceptually similar to non-stationary Metabolic Flux Analysis (MFA) [127,128]. Applied to HeLa cells, we derived a first comprehensive and quantitative view of metabolic flux oscillations at a high temporal resolution in central metabolism throughout the cell cycle of human cells, showing complementary oscillations between glucose and glutamine-derived flux in the TCA cycle throughout the cell cycle. Cell cycle dependent changes in flux through the pentose-phosphate pathway were previously studied using isotope tracing in synchronized human cell lines [129] and in yeast by also utilizing MFA [130].

The inferred flux oscillations through central metabolism via glucose and glutamine could potentially be biased by oscillations in the metabolism of other carbon sources. For example, the uptake and catabolism of glucogenic and ketogenic amino acids may feed into TCA cycle

and potentially oscillate through the cell cycle. Though, apparently, the relative contribution of amino acid catabolism to TCA cycle flux in HeLa cells is extremely low; feeding isotopic glucose and glutamine for 24h shows that more than 97% of the carbons in TCA cycle metabolites are derived exclusively from glucose and glutamine (and from atmospheric CO_2; Figure 29). Hence, a potential change in amino acid metabolism throughout the cell cycle would have little or no effect on the reported flux oscillations from glucose and glutamine. Not accounting for potential oscillations through other reactions implicated in central metabolism of glucose and glutamine could in principle also bias the presented flux estimations. Though, notably, the flux analysis here is performed separately through groups of converging reactions producing different metabolites (e.g. for reactions producing citrate, malate/oxaloacetate, lactate, etc.), hence a potential bias in some of these independent flux estimations would not change the overall emerging view of glucose and glutamine oscillations; e.g. the increased TCA cycle metabolism of glutamine in S phase is supported by several independent flux estimations showing increased glutamine-derived flux into TCA cycle in S phase, oxidation of α-ketoglutarate, reduction of α-ketoglutarate, malic enzyme flux, and increased nucleotide biosynthesis. Another simplifying assumption that facilitated the estimation of flux dynamics throughout the cell cycle is of rapid mixing of mitochondrial and cytosolic metabolite pools, giving rise to estimates of whole-cell level fluxes. This assumption is typically made when analyzing flux in eukaryotic cells due to experimental complications in measuring metabolite concentrations and labelling dynamics in distinct subcellular compartments. Methodological advancements in subcellular level metabolomics are required for further studies on cell cycle oscillations in metabolic flux in mitochondria versus cytosol.

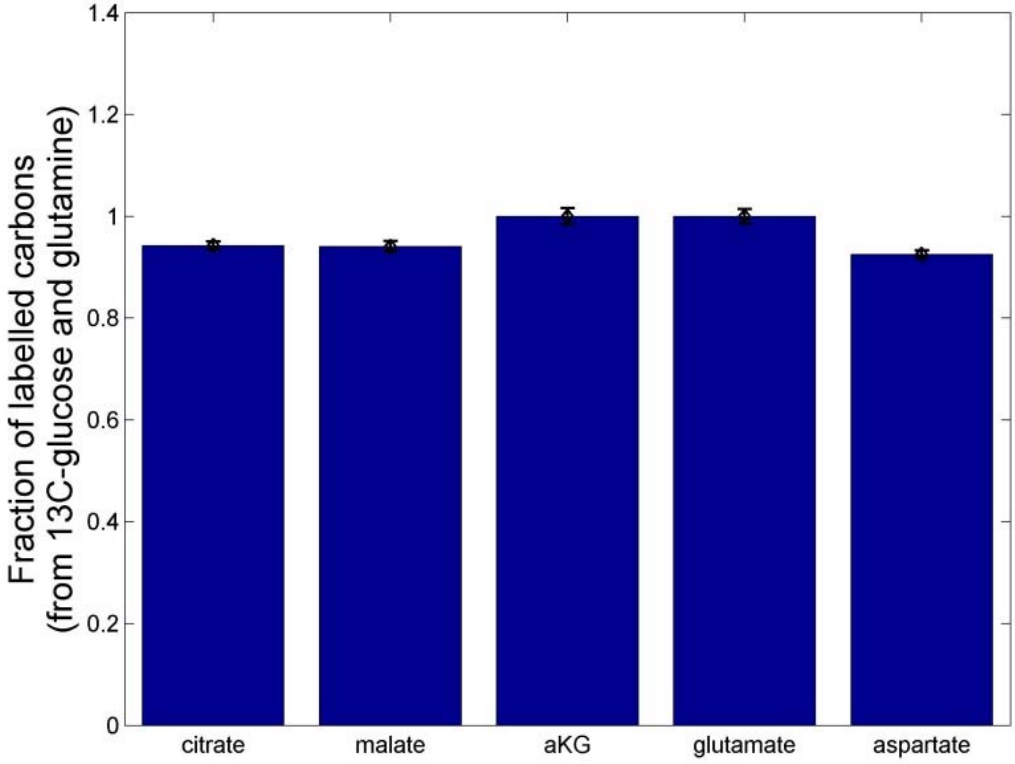

Figure 29: The fraction of carbons labeled in TCA cycle intermediates and other metabolites when feeding both [U-^{13}C]-glucose and [U-^{13}C]-glutamine for 24h. Additional carbons are derived from the fixation of atmospheric CO_2 through reductive isocitrate dehydrogenase (IDH) and pyruvate carboxylase (PC). E.g. for citrate, the fraction of citrate m+5 when feeding isotopic glutamine (as an indication of reductive IDH activity) and malate m+3 when feeding isotopic glucose (as an indication pyruvate carboxylase activity) suggest that another ~3% of the citrate carbons are derived from CO_2 fixation.

Our result of an induced glycolytic flux in G1/S phase is qualitatively consistent with previous reports ~3 to 10-fold increase in glycolytic flux in G1/S in HeLa cells [91,115]. However, here, analyzing the metabolism of synchronized cells after resuming exponential growth (i.e.

completing an entire cell cycle after released from synchronization growth-arrest), suggests a moderate increase in glycolytic flux of only ~65% in G1/S phase. The smaller magnitude of the oscillations in glycolytic flux inferred here is in agreement with the moderate changes in concentration of glycolytic intermediates, which increase only ~2-fold in G1/S phase. Our finding of increased glutamine-derived flux into the TCA cycle and support of pyrimidine biosynthesis in S phase agree with reports of the essentiality of glutamine (and not glucose) for entering and progressing through S phase, which can be rescued by nucleotide feeding [115,123].

We showed that complementary oscillations in the rate of glucose versus glutamine oxidation in the TCA cycle result in a constant rate of NADH/$FADH_2$ production and reduction of oxygen by the electron transport chain throughout the cell cycle. Notably, while here we observe a constant rate of oxygen consumption throughout the cell cycle, fluctuations in oxygen consumption were previously reported in yeast cells, with DNA replication and cell division occurring when oxygen consumption rate is low, protecting genome integrity [114]. On the other hand, respiration was suggested to actually protect against oxygen-associated DNA damage in proliferating human cells by reducing the intracellular oxygen concentration and ROS levels [131], and hence may potentially be beneficial during S phase. Cell cycle dependent changes in the utilization of glucose versus glutamine may be associated with reported changes in mitochondrial structure throughout the cell cycle, converted from isolated fragments into a hyperfused network in G1/S transition [132].

While the current study focuses on identifying and quantifying oscillations in metabolic flux throughout the cell cycle, further research is required to decipher how these metabolic changes are regulated. The ubiquitin ligase complexes APC/C and SCF complex were claimed to control glycolytic flux by limiting the expression of PFKFB3 to the G1/S transition, in accordance with the identified increase in glycolytic flux. SCF complex further limits the expression of GLS1 to S and G2/M phases, in agreement with our finding of induced

glutamine to glutamate conversion in these cell cycle phases. More generally, metabolic enzymes are typically not regulated at the level of mRNA or protein throughout the cell cycle based on cell cycle transcriptomics and proteomics studies [133]. However, post-translational modification of central metabolic enzymes is highly abundant and oscillations in phosphorylation levels of metabolic enzymes have been described [133]. Considering our finding of oscillations in the concentration of numerous metabolic intermediates, as well as energy and redox cofactors suggests that metabolic regulation via changes in enzyme-binding site occupancy and allosteric regulation may also play a key role in regulating cell cycle flux dynamics. This is further supported by the fact that metabolic substrate and inhibitor levels in mammalian cells are typically in the same range as the K_m values for the corresponding enzymes [134].

We showed that treatment of HeLa cells with the PDK inhibitor DCA eliminates the oscillations in glucose flux into TCA cycle, suggesting that cell cycle specific regulation of PDH activity may be involved in regulating these flux oscillations. Consistently, PDK4 was reported to be induced by the E2F-pRB pathway which controls cell entry to S phase [78,94]. Furthermore, analyzing published phosphoproteomics data for HeLa cells measured throughout the cell cycle [133] shows more than 2-fold increase in the phosphorylation of the PDH E1 component in early and late S phase versus in G1 (Figure 30). Validating this observation here, we find a significant 2-fold increase in the phosphorylation of PDH- S232 specifically in S phase (Figure 31). A drop in glycolytic flux into TCA cycle in S phase is further supported by a recent report of a drop in the abundance of the pyruvate-dehydrogenase complex in mitochondria in S phase, following translocation of the complex components to the nucleus [84]. Further research is required to determine the precise regulatory mechanism that underlies cell cycle oscillations in glycolytic flux into TCA cycle, which may potential spread quantitatively among several enzymes (in accordance with the view of Metabolic Control Analysis [135]).

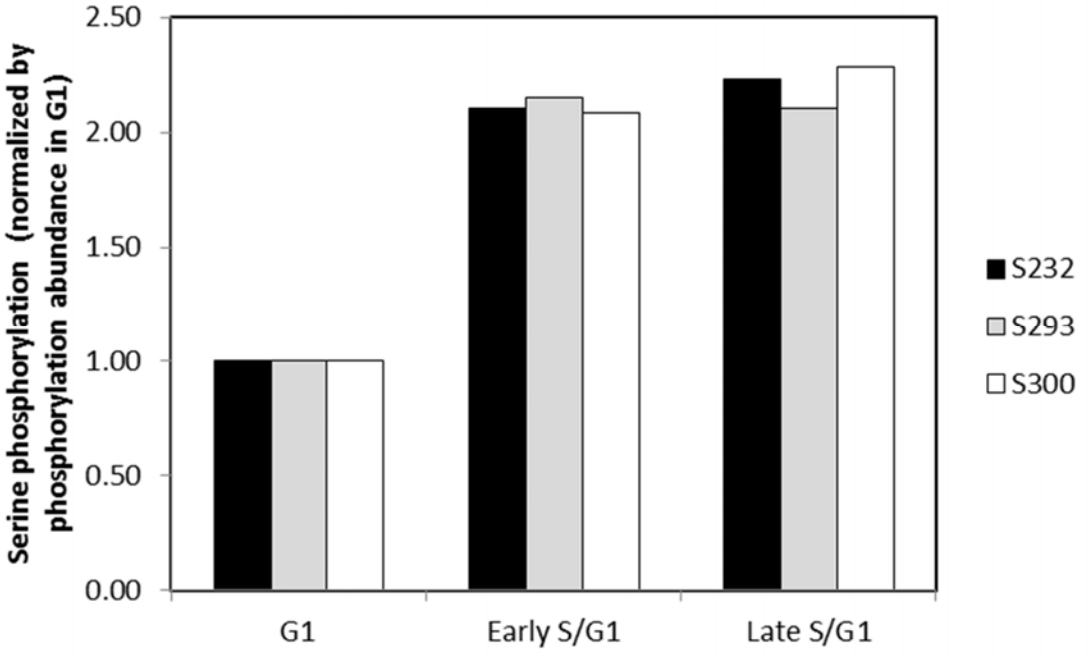

Figure 30: Abundance of PDH E1 phosphorylation increases in early and late S versus in G1 in all three reported phosphorylation sites (data from Olsen, J. V, *Sci Signal* **3,** 2010).

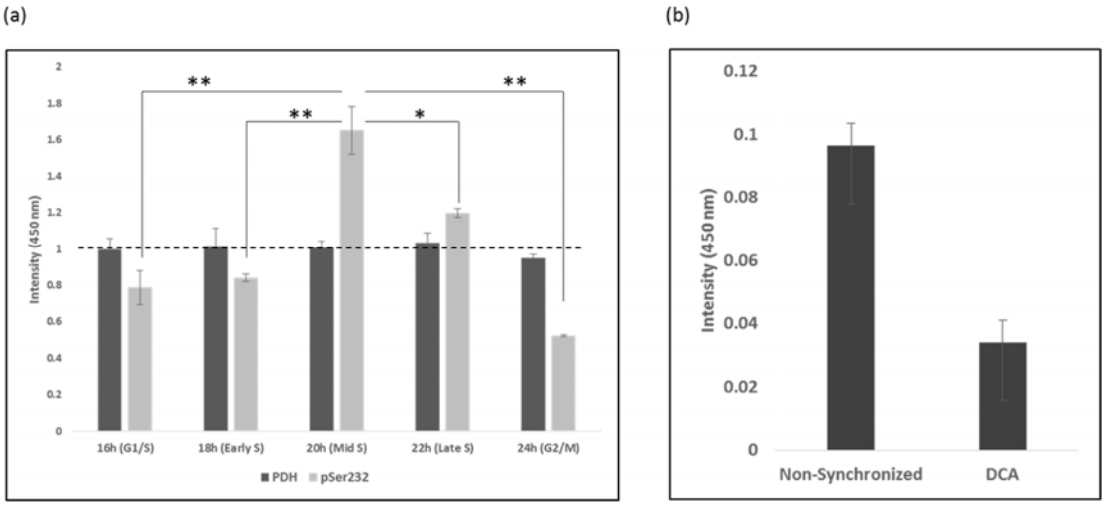

Figure 31: The phosphorylation at Ser232 of PDH seems to be related with the observed decreased glycolytic flux into TCA cycle in S phase. (a) Phosphorylation of PDH Ser232

increases in S phase. HeLa cells were synchronized using double thymidine block and lysates were prepared at different stages of the cell cycle. PDH phosphorylation was measured via an ELISA kit. All experiments were done in triplicates; two tailed Student's T-test was applied to calculate *p*-values. Notably, the concentration of PDH (measured via an ELISA kit) remains constant throughout the cell cycle. (b) DCA treatment significantly decreases PDH phosphorylation at Ser232.

In the conventional view of mammalian metabolism, acetyl-CoA (a major anabolic precursor for fatty acid biosynthesis) is primarily produced by the oxidation of glucose-derived pyruvate in mitochondria. Previous studies have employed isotope tracers to show that in cancer cells grown under hypoxia [136], in cells with defective mitochondria [137], and in anchorage-independent growth [138], a major fraction of acetyl-CoA is produced via another route, reductive carboxylation of glutamine-derived α-ketoglutarate (catalysed by reverse flux through isocitrate dehydrogenase, IDH). Under these conditions, feeding cells with isotopic glutamine leads to a marked increase in the fractional labeling of citrate m+5 and consequently in the isotopic labeling of synthesized fatty acids. Here, we showed that the fractional labeling of citrate m+5 significantly oscillates throughout the cell cycle under standard normoxic conditions. This reflects major oscillations in the relative contribution of oxidative TCA cycle flux (peaking in G1) and in the reductive metabolism of glutamine-derived α-ketoglutartate (peaking in S) to the production of acetyl-CoA throughout the cell cycle. Notably though, the oxidative IDH flux remains several-fold higher than the reductive flux all throughout the cell cycle, reflecting an overall net flux in the oxidative direction.

Understanding the metabolic adaptation of cells to tumorigenic mutations is a central goal of cancer metabolic research. Considering that tumorigenic mutations typically alter cell cycle progression, flux alterations observed at a cell population level may merely reflect a change in the distribution of cell-cycle phases in the population (due to cells in different phases having different metabolic fluxes). Hence, the presented temporal-fluxomics

approach will enable to revisit our understanding of oncogene-induced metabolic alterations, disentangling population level artifacts from directly regulated flux alterations with important tumorigenic role and revealing potential targets for therapy. Combined targeting of cell cycle specific flux alterations with drugs that block progression through the same cell cycle phases is expected to have important therapeutic applications [139,140].

4. Methods

5.1 Cell culture and synchronization

HeLa cells were cultured in Dulbecco's Modified Eagle Medium (high glucose, Biological Industries, 01-055-1A) supplemented with 10% (v/v) heat-inactivated dialyzed fetal bovine serum (Biological Industries), 3mM L-glutamine, 100U/mL penicillin, and 100µg/mL streptomycin with 5% CO_2 in a humidified incubator at 37°C. Culture medium was additionally supplemented with 84mg/mL L-serine, and 48mg/mL L-cystine to maintain sufficient amount of nutrients for three cell doublings. HeLa cells have been validated by the vendors and we tested for mycoplasma using EZ-PCR Mycoplasma detection kit (Biological Industries). Cell number and volume analysis was performed using a Z2 Beckman Coulter Counter (100 µm aperture); cells were trypsinized and resuspended in IsoFlow Sheath Fluid (Beckman Coulter) immediately before counting.

Cell synchronization was achieved using double thymidine block. Briefly, 2mM Thymidine (Sigma-T1895) was added to 10cm culture plates at 25-30% confluence for 17h. Cells were released from the first block by washing twice with phosphate buffer saline (PBS) and replacing with fresh culture medium. After 9h, cells were incubated with 2mM thymidine for a second block time for 17h. Cells were replated in smaller plates (60mm or 35mm) for further analysis. Cell cycle analysis of synchronized cells was performed by quantitation of DNA content using propodium iodide (PI) staining followed by flow cytometry. For PI staining, cells were fixed using 75% Ethanol/PBS and then resuspended in 0.5mL of PI staining solution (3.8mM sodium citrate, 40µg/mL PI, 50ng/mL RNase A) for 40 minutes at room temperature in dark. Flow cytometric analysis was performed using LSRII (BD Biosciences; with at least 50,000 cells per FACS run). Cell cycle stages from raw FACS data were quantified using Modfit (Verity House Software).

To check the effect of dicholoroacetate treatment on cell cycle progression, synchronized cells were treated with 4mM pyruvate dehydrogenase kinase inhibitor dichloroacetate (Sigma-Aldrich) for 3h. Non-synchronized cells were treated with 16mM DCA for 24h, followed by cytometric analysis after DNA staining with PI.

5.2 LC-MS based metabolomics and isotope tracing

To measure intracellular metabolite pools, cells were washed with 2ml of ice-cold PBS for three times and metabolites extracted with 200 µl of 50:30:20 (v/v/v) methanol:acetonitrile:water solution at -20°C. The cells were quickly scraped on dry ice. For the extraction of metabolites from the culture medium, 50µl of media were mixed with 200µl of 50:30 (v/v) methanol:acetonitrile solution at -20°C. All metabolite extractions were stored at -80°C for at least 1h, followed by centrifugation, twice at 20000g for 20 minutes to obtain protein-free metabolite extraction.

Metabolite pool sizes are expressed per total cell volume, measured using a Coulter counter in cells grown in parallel in different plates. Absolute metabolite concentrations for specific metabolites of interest were determined based on isotope ratio using chemical standards[141] (Dataset EV3). Pulse isotopic labelling was performed by feeding synchronized cells at each time point with either [U-^{13}C]-glucose or [U-^{13}C]-glutamine for 1 hr. To minimize the perturbation to cells due to the replacement with fresh media, we used conditioned medium obtained from a previous culture of HeLa cells. Specifically, conditioned medium with either isotopic glucose or isotopic glutamine was incubated with fully attached HeLa cells at ~30% confluence for 4 hours, and then stored in 4°C until used for pulse chase labeling experiments.

Chromatographic separation was achieved on a SeQuant ZIC-pHILIC column (2.1 × 150 mm, 5 µm bead size, Merck Millipore). Flow rate was set to 0.2 ml/min, column compartment was set to 30 °C and autosampler tray was maintained at 4°C. Mobile phase A consisted of

20 mM ammonium carbonate with 0.01% (v/v) ammonium hydroxide. Mobile Phase B was 100% acetonitrile. The mobile phase linear gradient (%B) was as follows: 0 min 80%, 15 min 20%, 15.1 min 80%, 23 min 80%. A mobile phase was introduced to Thermo Q-Exactive mass spectrometer with an electrospray ionization source working in polarity switching mode. Metabolites were analyzed using full-scan method in the range 70 - 1000 m/z and with a resolution of 70000. Positions of metabolites in the chromatogram were identified by corresponding pure chemical standards. Data were analyzed with MAVEN[142].

5.3 Measurement of oscillations in oxygen consumption

Measurement of oxygen consumption was done using the XFp Extracellular Flux analyzer (Agilent). Briefly, HeLa cells after synchronization were plated (20,000 cells/well) into XFp culture mini plates and grown at 37°C with 5% CO_2 in a humidified incubator for various times to enrich the cell population with cells at distinct cell cycle phases. Cells were washed and incubated with pre-warmed XF assay medium (Sigma D5030, pH 7.4) supplemented with 25mM glucose and 3mM glutamine for 1h in a non-CO_2 incubator at 37C. Appropriate dilutions of the inhibitors (final well concentrations: oligomycin 1 µM, FCCP 1 µM, rotenone/antimycinA 1 µM) were prepared in the assay medium as per the instructions in the manual. Hydrated sensor cartridges were calibrated prior to the measurement on SeaHorse XFp Extracellular Flux anylyzer (Agilent). Data acquisition consisted of a baseline measurement followed by oligomycin, FCCP and rotenone/antimycin A injections respectively. OCR data were normalized against cell volume obtained from Coulter counter measurements of the cells from a parallel plate without any treatment and expressed in pmoles/min/µl.

5.4 Synchronization loss model

We construct a probabilistic model that describes the loss of synchronization following release from double thymidine block, due to cell-cell variability in the rate of progression through the cell cycle. Each cell is assumed to have its own "internal clock", which controls the speed at which it progresses through the cell cycle (denoted by γ). The relative progression rates of cells released from synchronization arrest are assumed to be normally distributed: $\gamma \sim N(1, \sigma^2)$. We estimate the variance of the distribution (σ^2) as well as the duration of G1, S, and G2/M (denoted by d_G, d_S, and d_M, respectively; in hours), given the FACS measurements of the fraction of cells in each cell cycle phase in the synchronized cell population (as described below). We denote the cell doubling time by d_{CYC} ($=d_G+d_S+d_M$; in hours). For a cell whose rate of progression through the cell cycle is γ, the cell-intrinsic time x (in hours) within the cell cycle ($0 \leq x \leq d_{CYC}$) at time t post the release from synchronization-induced growth arrest is:

$$x = \gamma \cdot t + d_G - \left\lfloor \frac{(\gamma \cdot t + d_G)}{d_{CYC}} \right\rfloor d_{CYC}, \qquad \text{(Eq. 1)}$$

considering that cells resume growth in G1/S transition after released from double thymidine block. E.g. for a cell with a relative progression rate through the cell cycle of γ=1 released from growth arrest, it will take d_S+d_M hours to complete one cell cycle (and then have an intrinsic time of x=0), while for a cell with double the rate (γ=2) it will take half the time (i.e. $(d_S+d_M)/2$). At time t post the release from synchronization arrest, a cell having an intrinsic time of x has a relative progression rate through the cell cycle γ equal to $\frac{1}{t}(x + k \cdot d_{CYC} - d_G)$, with k representing the number of completed cell cycles since the release from growth arrest (based on Equation 1). Hence, considering that γ is normally distributed, we can compute the number of cells in the synchronized population at time t whose cell-intrinsic time is x (denoted $g'(x,t)$) as:

$$g'(x,t) = \sum_{k=0}^{2} 2^k \cdot e^{\frac{-\left(\frac{x+k \cdot d_{CYC}-d_G}{t}-1\right)^2}{2\sigma^2}}, \qquad \text{(Eq. 2)}$$

considering values of *k* between zero and two, representing three complete cell cycle. We denote by $g(x,t)$ the probability density function of the number of cells at time *t* whose cell intrinsic time is *x*, with $g(x,t) = \frac{1}{C}\, g'(x,t)$, where *C* is a normalization factor. The expected fraction of the cells in S, G1, and G2/M phases at time *t* (denoted by $m_S(t)$, $m_G(t)$ and $m_M(t)$, respectively) are calculated as:

$$m_S(t) = \int_0^{d_S} g(x,t)dx \qquad \text{(Eq. 3)}$$

$$m_G(t) = \int_{d_S}^{d_S+d_G} g(x,t)dx \qquad \text{(Eq. 4)}$$

$$m_M(t) = \int_{d_S+d_G}^{dCYC} g(x,t)dx \qquad \text{(Eq. 5)}$$

We perform a maximum log-likelihood estimation of the four parameters of the model (σ, d_G, d_S, and d_M), minimizing the variance-weighted sum of squared residuals between the simulated fraction of cells in the different cell cycle phases ($m_S(t)$, $m_G(t)$ and $m_M(t)$) and the FACS measurements (assuming Gaussian noise in FACS measurements with an empirically estimated standard deviation of ~10%). This minimization was performed via an implementation of sequential quadratic optimization (SQP) available in Matlab. Confidence intervals were computed by the likelihood ratio test, comparing the maximum log-likelihood estimates with that obtained when constraining each of the four parameters to increasing and then decreasing value (considering the 95% quantile of χ^2-distribution with one degree of freedom). The optimal parameters found were σ=11%±1%, d_G=6.8h±0.8h, d_S=6.4h±0.5h, and d_M=3.2h±0.4h. Overall, the good fit between the model prediction and experimental data shown in Figure 1b supports the underlying assumptions of this model. Computing the duration of each cell cycle phase based on PI staining/FACS measurements in a population of non-synchronized HeLa cells, and considering a decreasing exponential cell age distribution shows 8.2h for G1, 4.9h for S, and 2.9h for G2/M. The small under estimation of the duration of G1 and over estimation of the duration of S by the analysis of the synchronized cell (both not more than 1h off the measurements in the non-

synchronized cells) may be due to a slight perturbation to cell cycle dynamics due to synchronization-induced growth arrest.

5.5 Computational deconvolution of cell volume measurements in the synchronized cell population:

Computational deconvolution was used to estimate cell volume dynamics throughout the cell cycle, correcting for cell dispersion that bias Coulter counter measurements of cell volume performed in the synchronized cells. Specifically, denoting the average cell volume in the synchronized cell population at time *t* by $v(t)$ ($9 \leq t \leq 45$), we estimate the average cell volume in the cell-intrinsic time *x* within the cell cycle ($0 \leq x \leq d_{CYC}$), denoted by $\mathrm{v}'(x)$, as following:

$$v(t) = \int_0^{d_{CYC}} v'(x) g(x,t) dx + \varepsilon(t), \qquad \text{(Eq. 6)}$$

where $\varepsilon(t)$ represents experimental noise in the volume measurement performed at time t. We represent $v'(x)$ using a cubic spline, which is a commonly used approach for fitting biological time-series data (considering splines with 4 segments; defined based on 5 knots). Non-convex optimization was used to find the optimal position of the knots and corresponding value of $v'(t)$ minimizing the sum-of-square of the error terms. Non-convex optimizations were solved using Matlab's implementation of SQP.

5.6 Computational deconvolution of metabolite concentration, isotope labeling, and uptake and secretion rate measurements

Given a metabolite *I,* whose measured concentration in the synchronized cell population at time t ($9 \leq t \leq 45$) is denoted by $u_i(t)$ (measured metabolite pool size normalized by the

measured average cell volume at time t; $v(t)$), we estimate the concentration in cell-intrinsic time x within the cell cycle ($0 \leq x \leq d_{CYC}$), denoted by $u_i'(x)$ as:

$$u_i(t) = \frac{1}{\int_0^{d_{CYC}} v\prime(x)g(x,t)dx} \int_0^{d_{CYC}} u_i'(x)v'(x)g(x,t)dx + \varepsilon(t), \qquad \text{(Eq. 7)}$$

considering that the measured concentration of metabolite *i* at time *t* represents the average concentration in cells with cell-intrinsic time *x*, weighted by the total volume of cells with intrinsic time *x* at time *t* (i.e. $v'(x)g(x,t)$). We represent $u_i'(x)$ using a cubic spline and estimate its coefficients as described above.

We denote the measured relative abundance of the k^{th} mass isotopomer of metabolite *i* (i.e. the fraction of the metabolite pool having *k* labeled carbons) after one hour feeding with an isotopic substrate of synchronized cells at time *t* by $u_{i,k}(t)$. We estimate the relative abundance of the k^{th} mass isotopomer of metabolite *i* in cell-intrinsic time x within the cell cycle denoted $u_{i,k}'(x)$ as:

$$u_{i,k}(t) = \frac{1}{\int_0^{\infty} u_i'(x)v\prime(x)g(x,t)dx} \int_0^{\infty} u_{i,k}'(x)u_i'(x)v'(x)g(x,t)dx + \varepsilon(t), \qquad \text{(Eq. 8)}$$

considering that the measured fractional isotopic labeling of a metabolite *i* at time *t* represents the average labeling in cells with intrinsic cell cycle time *x*, weighted by the metabolite pool size in cells with cell-intrinsic time *x* (i.e. with $u_i'(x)v'(x)g(x,t)$).

We denote the measured change in pool size of metabolite *i* in the culture media between time $t - \Delta t$ and time t by $\Delta e_i(t)$. We estimate the transport flux of metabolite *i* by the synchronized cell population at time *t*, denoted $f_i(t)$ (in molar amount per unit of cell volume per hour; with positive and negative flux representing secretion and uptake, respectively) by dividing the change in pool size of metabolite *i* by the accumulated volume of cells in the culture metabolite between time $t - \Delta t$ and time t:

$$f_i(t) = \frac{1}{\int_{t-\Delta t}^{t} \int_0^{d_{CYC}} v\prime(x)g(x,t\prime)dxdt\prime} \Delta e_i(t) \qquad , \qquad \text{(Eq. 9)}$$

The transport flux of metabolite *i* at cell-intrinsic time *x*, denoted $f_i'(x)$ is estimated as:

$$\Delta e_i(t) = \int_{t-\Delta t}^{t} \int_0^{d_{CYC}} f_i'(x)\, v'(x) g(x,t') dx\, dt' + \varepsilon(t), \quad \text{(Eq. 10)}$$

considering that the measured change in pool size of metabolite *i* at time *t* represents the cumulative transport within the Δt time interval by cells with different intrinsic cell cycle time *x*.

5.7 Statistical significance of oscillations in metabolite concentrations and isotopic labeling patterns:

To assess the statistical significance of observed oscillations in the deconvoluted concentration of a certain metabolite, we compared the observed amplitude of the oscillation to the amplitude expected by chance (considering the noise in LC-MS measurements). Specifically, for each metabolite *i*, we define the amplitude of its oscillation by a_i as:

$$a_i = \max_{0 \le x \le d_{CYC}} u_i'(x) - \min_{0 \le x \le d_{CYC}} u_i'(x) \quad \text{(Eq. 11)}$$

Next, we compute the distribution of amplitudes expected by chance by repeating the following steps 10,000 times: For each time t for which LC-MS measurements were performed on the synchronized cell population ($9 \le t \le 45$), we generate a random metabolite concentration (denoted $\mathrm{r}(t)$) by sampling from a normal distribution whose mean is the average concentration of metabolite *i* measured throughout all time points in the synchronized cells, and with the standard deviation of the experimental measurement of metabolite *i* at time *t*, denoted $\sigma_i(t)$:

$$r(t) \sim N\left(\frac{1}{k}\sum_{t=1}^{k} u_i(t)\,, \sigma_i^2(t)\right). \quad \text{(Eq. 12)}$$

Computational deconvolution (Eq. 7) is applied on the randomly generated metabolite concentration data (i.e. *r*(t)) and an empirical *p*-value computed based on the fraction of randomly sampled concentration vectors for which the derived amplitude is equal or larger

than that computed for the concentration measurements of metabolite *i*. FDR correction for multiple testing is computed using the approach of Benjamini–Hochberg. A conceptually similar method was employed to assess the statistical significance of oscillations in the relative abundance of metabolite isotopic labeling (applying computational deconvolution (Eq. 8) to randomly generated isotopic labelling data).

5.8 Computational inference of metabolic flux dynamics throughout the cell cycle:

For every one-hour interval *j* throughout the cell cycle $j \in \{0 \dots \lfloor d_{CYC} \rfloor\}$ (referred to as the *j*th *cell cycle interval*), we computed the most likely momentary fluxes through 9 reactions in TCA cycle and in branching pathways (Figure 11b). Towards this end we employed a variant of Kinetic Flux Profiling (KFP) to separately infer fluxes producing each metabolite *i* in cell cycle interval *j*, for which the simulated isotopic labeling kinetics optimally match the experimental measurements.

The relative abundance of the *k*th mass-isotopomer of metabolite *i* after 1 hour feeding of cells within cell cycle interval *j* was inferred based on the pulse chase labeling experiments in the synchronized cells followed by deconvolution as described above (denoted by $u'_{i,k}(j)$). To estimate the dynamics of the isotopic labeling form of this metabolite within the one-hour cell cycle interval (i.e. within time periods shorter than one hour), we performed pulse-chase labeling experiments with isotopic glucose and glutamine in non-synchronized cells, measuring the relative abundance of the *k*th mass-isotopomer of metabolite *i* at different times $t \in T = \{10,20,30,60\}$ (in minutes), denoted by $X_{i,k}(t)$. These measurements were used to estimate the relative abundance of the *k*th mass-isotopomer of metabolite *i*, *t* minutes after the beginning of the *j*th one-hour time interval within the cell cycle (denoted by $X^{j}_{i,k}(t)$) by scaling the measurements performed on the non-synchronized cells:

$$X_{i,k}^{j}(t) = \frac{u'_{i,k}(j+1)}{X_{i,k}(60)} X_{i,k}(t) \qquad \text{(Eq. 13)}$$

To validate these estimated labeling kinetics, we performed rapid pulse-chase labeling experiments (10 and 30 minutes) in synchronized cells grown for 15 hours (G1/S) and 20 hours (S), finding a good match between the estimated and measured labeling dynamics (Figure 32).

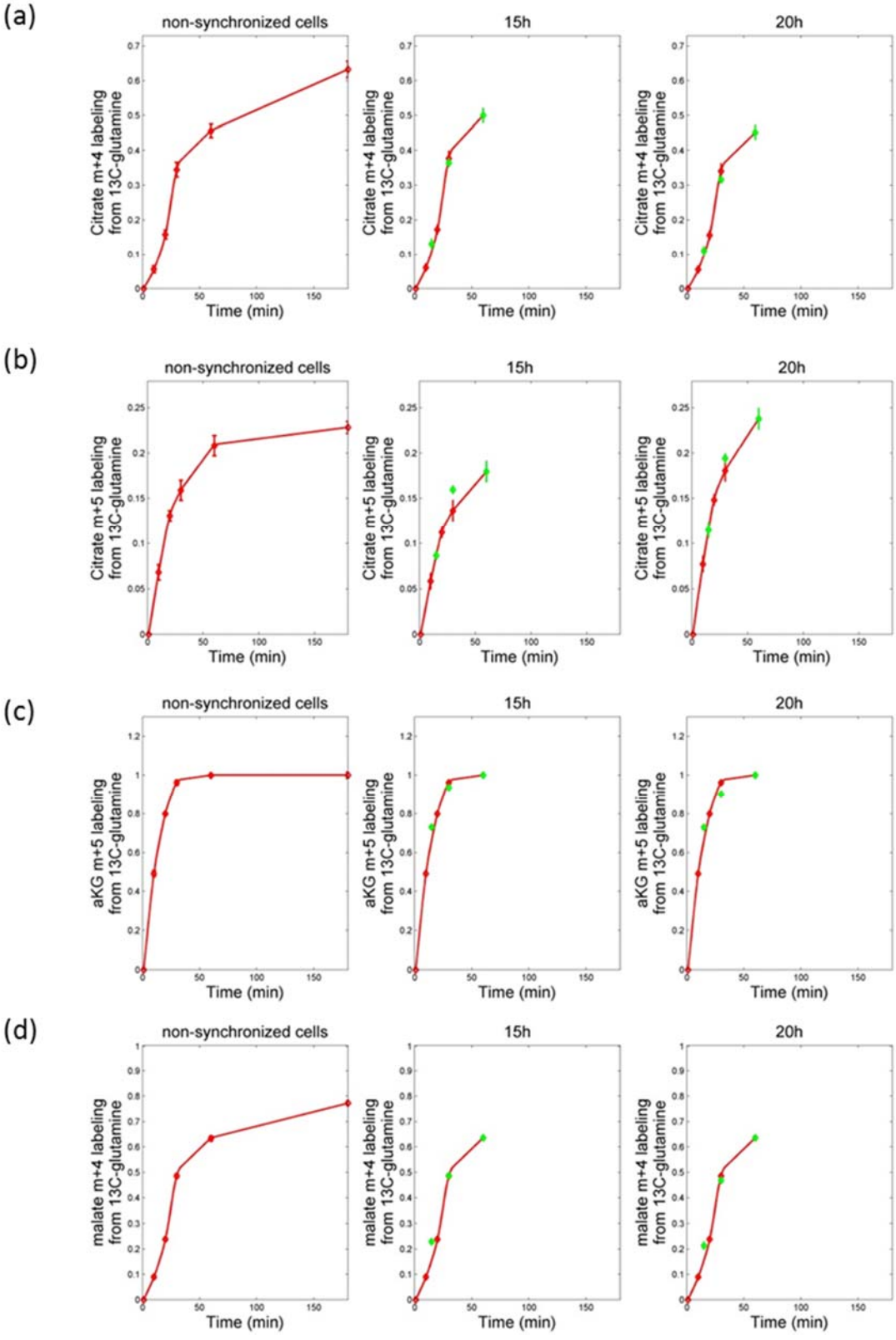

Figure 32: The estimated and measured short-time (10 and 30 mins) labeling kinetics for 15 and 20 hours show a good match. (a) Measured (green dots) versus estimated (red curves) labeling kinetics of citrate m+4 (a), citrate m+5 (b), α-ketoglutarate m+5 (c), and malate m+4 (d), when feeding non-synchronized and synchronized cells in G1/S (15h) and S (20h) with isotopic glutamine. The estimated labeling kinetics in the synchronized cells was derived based on Eq. 13 (in main text).

We describe the inference of metabolic flux through reactions producing citrate while other fluxes are obtained similarly (see below). The analysis accounts for citrate synthase (v_1) and reductive isocitrate dehydrogenase (IDH; v_2) producing citrate (Figure 11b). We denote the total citrate consumption flux by v_{out}, which may be lower or higher than the sum of *v1* and *v2* in case citrate is accumulated or depleted within a cell cycle interval, respectively (as the synchronized cells are not in metabolic steady-state). The expected mass-isotopomer distribution of citrate after *t* minutes into the j^{th} cell cycle interval, considering the fluxes *v1*, *v2*, and v_{out} is denoted $Y_{cit}^{j}(t, v_1, v_2, v_{out})$. Assuming that the error in the measured isotope labeling data is normally distributed, maximum likelihood estimate of fluxes are obtained by minimizing the variance-weighted sum of squared residuals between measured and computed mass-isotopomer distributions, where $\sigma_{cit,k}^{j}$ is the standard deviation in the measurement of the relative abundance of the k^{th} mass-isotopomer of citrate in the j^{th} time interval:

$$\min_{v_1,v_2,v_{out}} \sum_{t\in T} \sum_{k\epsilon\{4,5\}} \left(\frac{X_{cit,k}^{j}(t) - Y_{cit,k}^{j}(t,v_1,v_2,v_{out})}{\sigma_{cit,k}^{j}} \right)^2 \qquad \text{(Eq. 14)}$$

s.t.

$$v_{out} = v_1 + v_2 + \left(u'_{cit}(j+1) - u'_{cit}(j)\right) \qquad \text{(Eq. 14.1)}$$

$$v_1, v_2, v_{out} \geq 0 \qquad \text{(Eq. 14.2)}$$

Where $u'_{cit}(j)$represents the deconvoluted concentration of citrate (in mM) in the j^{th} cell cycle interval, and is used to constrain the difference between the total citrate producing and consuming flux within the j^{th} one-hour cell cycle interval (Eq. 14.1). We accounted for the two major mass-isotopomers of citrate, m+4 and m+5 (Figure 13). To simulate the labeling kinetics of the k^{th} mass-isotopomer of citrate within the j^{th} cell cycle interval, denoted by $Y^{j}_{cit,k}(t, v_1, v_2, v_{out})$, we utilized the following system of ordinary differential equations (Eq. 14.3):

$$\frac{dY^{j}_{cit,k}(t, v_1, v_2, v_{out})}{dt} = \frac{1}{u'_{cit}(j)}\left(v_1 X^{j}_{mal,k}(t) + v_2 X^{j}_{aKG,k}(t) - v_{out} Y^{j}_{cit,k}(t, v_1, v_2, v_{out})\right)$$

where $X^{j}_{mal,k}(t)$ and $X^{j}_{aKG,k}(t)$ represent the relative abundance of the k^{th} mass-isotopomer of malate and α-ketoglutarate, *t* minutes into the j^{th} cell-cycle interval; and $v_1 X^{j}_{mal,k}(t)$ and $v_2 X^{j}_{aKG,k}(t)$ represent the momentary production of the k^{th} mass-isotopomer of citrate from of malate and from α-ketoglutarate. The term $v_{out} Y^{j}_{cit,k}(t, v_1, v_2, v_{out})$ represents the total momentary consumption of the k^{th} mass-isotopomer of citrate. The difference between the momentary production and consumption rate of the different mass-isotopomers of citrate (term in parenthesis on right hand side of the equation) is normalized by the concentration of citrate to give the momentary change in fractional labeling.

A similar approach was employed to infer fluxes through reactions producing the following metabolites: (i*) α-ketoglutarate* – rapid isotopic exchange with glutamate results in essentially a single intracellular pool of α-ketoglutarate and glutamate (as reflected by similar labeling kinetics of the two metabolites). We considered α-ketoglutarate/glutamate m+5 production by oxidative IDH from citrate m+5 when feeding isotopic glutamine (reaction *v3* in Figure 11b) and from glutamine m+5 when feeding isotopic glutamine (*v8*), as well α-ketoglutarate/glutamate m+3 production by oxidative IDH from citrate m+4 when feeding isotopic glutamine (*v3*) (Figure 14). (ii) *Malate* – considering the rapid isotopic

exchange with aspartate (>100mM/h based KFP analysis of malate and aspartate labeling kinetics, we account for a single malate/aspartate pool. We consider for malate/aspartate m+4 production from α-ketoglutarate m+5 (*v4*), when feeding isotopic glutamine, and malate/aspartate m+4 production from pyruvate m+3 (*v7*), when feeding isotopic glucose (Figure 15). (iii) *UTP* – considering UTP m+3 production from carbamoyl-aspartate m+3 when feeding isotopic glutamine (*v5*) (Appendix Figure S6). (iii) *Lactate* – considering lactate m+3 production by malic enzyme when feeding isotopic glutamine (*v6*) and the production of non-labelled lactate by glycolysis (Figure 17). We consider an average malic enzyme flux of 7.9mM/h throughout the cell cycle (considering a fractional labeling of 1.3% m+3 lactate under isotopic steady state, when feeding isotopic glutamine; and lactate secretion rate of 610mM/h).

Non-convex optimizations were solved using Matlab's implementation of Sequential Quadratic Optimization (SQP). All optimizations were run 10 times, starting from different sets of random fluxes, to overcome potential local minima. To compute confidence intervals for estimated fluxes, we iteratively ran the SQP optimization to compute the maximum log-likelihood estimation while constraining the flux to increasing (and then decreasing) values (with a step size equal to 5% of the flux predicted in the initial maximum log-likelihood estimation)[125,143]. The confidence interval bounds were determined based on the 95% quantile of χ^2-distribution with one degree of freedom. Notably, while all flux estimates are given in mM/h (i.e. fmole/pL-cells/h), multiplying a flux estimate with intrinsic time *x* with the estimated cell volume at that time (i.e. $v'(x)$ in pL; see Figure 1c) gives a flux value per cell (fmole/cell/h).

The rate of production of reducing equivalents for driving oxidative phosphorylation generated by glucose oxidation was calculated by summing the flux through the following NADH producing reactions: PDH (according to reaction *v1* in Figure 11b; considering that ~99% of pyruvate is produced by glucose oxidation throughout the cell cycle, with the fractional labeling of pyruvate from isotopic glutamine under isotopic steady state being <

0.01), oxidative IDH (reaction *v3*), and the rate of shuttling of NADH produced in glycolysis for oxidation in mitochondria (estimated based on pyruvate secretion; a uniform flux of ~17mM/h measured throughout the cell cycle). The rate of reducing equivalents production from glutamine oxidation was calculated based on the rate of α-ketoglutarate oxidation in TCA cycle (reaction *v4* in Figure 11b; considering that >95% of α-ketoglutarate is produced from glutamine all throughout the cell cycle; the fractional labeling of α-ketoglutarate from isotopic glutamine under isotopic steady state is > 0.95), producing NADH by α-ketoglutarate dehydrogenase and $FADH_2$ by succinate dehydrogenase (SDH). Malate dehydrogenase (*v4* in Figure 11b) further produces another NADH.

References

1. Antoniewicz, M. R. Methods and advances in metabolic flux analysis: a mini-review. *J. Ind. Microbiol. Biotechnol.* **42,** 317–325 (2015).

2. Altschuler, S. J. & Wu, L. F. Cellular heterogeneity: when do differences make a difference? *Cell* **141,** 559–563 (2010).

3. Bar-Joseph, Z. *et al.* Genome-wide transcriptional analysis of the human cell cycle identifies genes differentially regulated in normal and cancer cells. *Proc Natl Acad Sci U S A* **105,** 955–960 (2008).

4. Siegel, R. L., Miller, K. D. & Jemal, A. Cancer statistics, 2018. *CA. Cancer J. Clin.* **68,** 7–30 (2018).

5. Cancer Progress Report. *Clinical cancer research : an official journal of the American Association for Cancer Research* **21,** S1-128 (2015).

6. Vander Heiden, M. G., Cantley, L. C. & Thompson, C. B. Understanding the Warburg effect: the metabolic requirements of cell proliferation. *Science (80-.).* **324,** 1029–1033 (2009).

7. Ward, P. S. & Thompson, C. B. Metabolic Reprogramming: A Cancer Hallmark Even Warburg Did Not Anticipate. *Cancer Cell* **21,** 297–308 (2012).

8. Vander Heiden, M. G. Targeting cancer metabolism: a therapeutic window opens. *Nat Rev Drug Discov* **10,** 671–684 (2011).

9. Frezza, C. *et al.* Haem oxygenase is synthetically lethal with the tumour suppressor fumarate hydratase. *Nature* **477,** 225–228 (2011).

10. Linardou, H., Dahabreh, I. J., Bafaloukos, D., Kosmidis, P. & Murray, S. Somatic EGFR

mutations and efficacy of tyrosine kinase inhibitors in NSCLC. *Nat Rev Clin Oncol* **6,** 352–366 (2009).

11. Normanno, N. *et al.* Implications for KRAS status and EGFR-targeted therapies in metastatic CRC. *Nat Rev Clin Oncol* **6,** 519–527 (2009).

12. Wallingford, R. A. & Ewing, A. G. Separation of serotonin from catechols by capillary zone electrophoresis with electrochemical detection. *Anal. Chem.* **61,** 98–100 (1989).

13. Pavlova, N. N. & Thompson, C. B. The Emerging Hallmarks of Cancer Metabolism. *Cell Metab.* **23,** 27–47 (2016).

14. Nicklin, P. *et al.* Bidirectional transport of amino acids regulates mTOR and autophagy. *Cell* **136,** 521–534 (2009).

15. Commisso, C. *et al.* Macropinocytosis of protein is an amino acid supply route in Ras-transformed cells. *Nature* **497,** 633–637 (2013).

16. Krajcovic, M., Krishna, S., Akkari, L., Joyce, J. A. & Overholtzer, M. mTOR regulates phagosome and entotic vacuole fission. *Mol. Biol. Cell* **24,** 3736–3745 (2013).

17. Stolzing, A. & Grune, T. Neuronal apoptotic bodies: phagocytosis and degradation by primary microglial cells. *FASEB J. Off. Publ. Fed. Am. Soc. Exp. Biol.* **18,** 743–745 (2004).

18. Kamphorst, J. J. *et al.* Hypoxic and Ras-transformed cells support growth by scavenging unsaturated fatty acids from lysophospholipids. *Proc. Natl. Acad. Sci. U. S. A.* **110,** 8882–8887 (2013).

19. Lunt, S. Y. & Vander Heiden, M. G. Aerobic glycolysis: meeting the metabolic requirements of cell proliferation. *Annu. Rev. Cell Dev. Biol.* **27,** 441–464 (2011).

20. Itkonen, H. M. *et al.* O-GlcNAc transferase integrates metabolic pathways to regulate the stability of c-MYC in human prostate cancer cells. *Cancer Res.* **73,** 5277–5287 (2013).

21. Jiang, P. *et al.* p53 regulates biosynthesis through direct inactivation of glucose-6-phosphate dehydrogenase. *Nat. Cell Biol.* **13,** 310–316 (2011).

22. Ying, H. *et al.* Oncogenic Kras maintains pancreatic tumors through regulation of anabolic glucose metabolism. *Cell* **149,** 656–670 (2012).

23. Wang, C. *et al.* Identification of transaldolase as a novel serum biomarker for hepatocellular carcinoma metastasis using xenografted mouse model and clinic samples. *Cancer Lett.* **313,** 154–166 (2011).

24. Zhang, J. *et al.* Asparagine plays a critical role in regulating cellular adaptation to glutamine depletion. *Mol. Cell* **56,** 205–218 (2014).

25. Casero, R. A. J. & Marton, L. J. Targeting polyamine metabolism and function in cancer and other hyperproliferative diseases. *Nat. Rev. Drug Discov.* **6,** 373–390 (2007).

26. Gerner, E. W. & Meyskens, F. L. J. Polyamines and cancer: old molecules, new understanding. *Nat. Rev. Cancer* **4,** 781–792 (2004).

27. Chiang, E.-P. I., Wang, Y.-C., Chen, W.-W. & Tang, F.-Y. Effects of insulin and glucose on cellular metabolic fluxes in homocysteine transsulfuration, remethylation, S-adenosylmethionine synthesis, and global deoxyribonucleic acid methylation. *J. Clin. Endocrinol. Metab.* **94,** 1017–1025 (2009).

28. Shyh-Chang, N. *et al.* Influence of threonine metabolism on S-adenosylmethionine and histone methylation. *Science* **339,** 222–226 (2013).

29. Killian, J. K. *et al.* Succinate dehydrogenase mutation underlies global epigenomic divergence in gastrointestinal stromal tumor. *Cancer Discov.* **3,** 648–657 (2013).

30. Letouze, E. *et al.* SDH mutations establish a hypermethylator phenotype in paraganglioma. *Cancer Cell* **23,** 739–752 (2013).

31. Colegio, O. R. *et al.* Functional polarization of tumour-associated macrophages by tumour-derived lactic acid. *Nature* **513,** 559–563 (2014).

32. Vegran, F., Boidot, R., Michiels, C., Sonveaux, P. & Feron, O. Lactate influx through the endothelial cell monocarboxylate transporter MCT1 supports an NF-kappaB/IL-8 pathway that drives tumor angiogenesis. *Cancer Res.* **71,** 2550–2560 (2011).

33. Swietach, P., Vaughan-Jones, R. D. & Harris, A. L. Regulation of tumor pH and the role of carbonic anhydrase 9. *Cancer Metastasis Rev.* **26,** 299–310 (2007).

34. Fallarino, F. *et al.* T cell apoptosis by tryptophan catabolism. *Cell Death Differ.* **9,** 1069–1077 (2002).

35. Fallarino, F. *et al.* The combined effects of tryptophan starvation and tryptophan catabolites down-regulate T cell receptor zeta-chain and induce a regulatory phenotype in naive T cells. *J. Immunol.* **176,** 6752–6761 (2006).

36. Opitz, C. A. *et al.* An endogenous tumour-promoting ligand of the human aryl hydrocarbon receptor. *Nature* **478,** 197–203 (2011).

37. Barthel, A. *et al.* Regulation of GLUT1 gene transcription by the serine/threonine kinase Akt1. *J. Biol. Chem.* **274,** 20281–20286 (1999).

38. Wieman, H. L., Wofford, J. A. & Rathmell, J. C. Cytokine stimulation promotes glucose uptake via phosphatidylinositol-3 kinase/Akt regulation of Glut1 activity and trafficking. *Mol. Biol. Cell* **18,** 1437–1446 (2007).

39. DeBerardinis, R. J. & Chandel, N. S. Fundamentals of cancer metabolism. *Sci. Adv.* **2,** (2016).

40. Xiao, D. *et al.* Myc promotes glutaminolysis in human neuroblastoma through direct activation of glutaminase 2. *Oncotarget* **6,** 40655–40666 (2015).

41. Astuti, D. *et al.* Gene mutations in the succinate dehydrogenase subunit SDHB cause susceptibility to familial pheochromocytoma and to familial paraganglioma. *Am. J. Hum. Genet.* **69,** 49–54 (2001).

42. Janeway, K. A. *et al.* Defects in succinate dehydrogenase in gastrointestinal stromal tumors lacking KIT and PDGFRA mutations. *Proc. Natl. Acad. Sci. U. S. A.* **108,** 314–318 (2011).

43. Tomlinson, I. P. M. *et al.* Germline mutations in FH predispose to dominantly inherited uterine fibroids, skin leiomyomata and papillary renal cell cancer. *Nat. Genet.* **30,** 406–410 (2002).

44. Ward, P. S. *et al.* The common feature of leukemia-associated IDH1 and IDH2 mutations is a neomorphic enzyme activity converting alpha-ketoglutarate to 2-hydroxyglutarate. *Cancer Cell* **17,** 225–234 (2010).

45. Dang, L. *et al.* Cancer-associated IDH1 mutations produce 2-hydroxyglutarate. *Nature* **465,** 966 (2010).

46. Thompson, C. B. Metabolic Enzymes as Oncogenes or Tumor Suppressors. *N. Engl. J. Med.* **360,** 813–815 (2009).

47. Zhou, B., Xiao, J. F., Tuli, L. & Ressom, H. W. LC-MS-based metabolomics. *Mol. Biosyst.* **8,** 470–481 (2012).

48. Pitt, J. J. Principles and Applications of Liquid Chromatography-Mass Spectrometry

in Clinical Biochemistry. *Clin. Biochem. Rev.* **30,** 19–34 (2009).

49. Fenn, J. B., Mann, M., Meng, C. K., Wong, S. F. & Whitehouse, C. M. Electrospray ionization for mass spectrometry of large biomolecules. *Science* **246,** 64–71 (1989).

50. Demarque, D. P., Crotti, A. E. M., Vessecchi, R., Lopes, J. L. C. & Lopes, N. P. Fragmentation reactions using electrospray ionization mass spectrometry: an important tool for the structural elucidation and characterization of synthetic and natural products. *Nat. Prod. Rep.* **33,** 432–455 (2016).

51. Zenobi, R. Single-Cell Metabolomics: Analytical and Biological Perspectives. *Science (80-.).* **342,** (2013).

52. Fessenden, M. Metabolomics: Small molecules, single cells. *Nature* **540,** 153 (2016).

53. Wakamoto, Y., Ramsden, J. & Yasuda, K. Single-cell growth and division dynamics showing epigenetic correlations. *Analyst* **130,** 311–317 (2005).

54. Kaern, M., Elston, T. C., Blake, W. J. & Collins, J. J. Stochasticity in gene expression: from theories to phenotypes. *Nat. Rev. Genet.* **6,** 451–464 (2005).

55. Colman-Lerner, A. *et al.* Regulated cell-to-cell variation in a cell-fate decision system. *Nature* **437,** 699–706 (2005).

56. Becskei, A., Kaufmann, B. B. & van Oudenaarden, A. Contributions of low molecule number and chromosomal positioning to stochastic gene expression. *Nat. Genet.* **37,** 937–944 (2005).

57. Wakamoto, Y. *et al.* Dynamic persistence of antibiotic-stressed mycobacteria. *Science* **339,** 91–95 (2013).

58. Fridman, O., Goldberg, A., Ronin, I., Shoresh, N. & Balaban, N. Q. Optimization of lag time underlies antibiotic tolerance in evolved bacterial populations. *Nature* **513,**

418–421 (2014).

59. Marusyk, A., Almendro, V. & Polyak, K. Intra-tumour heterogeneity: a looking glass for cancer? *Nat. Rev. Cancer* **12,** 323–334 (2012).

60. Brown, R., Curry, E., Magnani, L., Wilhelm-Benartzi, C. S. & Borley, J. Poised epigenetic states and acquired drug resistance in cancer. *Nat. Rev. Cancer* **14,** 747–753 (2014).

61. Gupta, P. B. *et al.* Stochastic state transitions give rise to phenotypic equilibrium in populations of cancer cells. *Cell* **146,** 633–644 (2011).

62. Nemes, P., Knolhoff, A. M., Rubakhin, S. S. & Sweedler, J. V. Metabolic differentiation of neuronal phenotypes by single-cell capillary electrophoresis-electrospray ionization-mass spectrometry. *Anal. Chem.* **83,** 6810–6817 (2011).

63. Nemes, P., Knolhoff, A. M., Rubakhin, S. S. & Sweedler, J. V. Single-cell metabolomics: changes in the metabolome of freshly isolated and cultured neurons. *ACS Chem. Neurosci.* **3,** 782–792 (2012).

64. O'Brien, P. J. *et al.* Monitoring metabolic responses to chemotherapy in single cells and tumors using nanostructure-initiator mass spectrometry (NIMS) imaging. *Cancer Metab.* **1,** 4 (2013).

65. Chandra, S. Quantitative imaging of chemical composition in single cells by secondary ion mass spectrometry: cisplatin affects calcium stores in renal epithelial cells. *Methods Mol. Biol.* **656,** 113–130 (2010).

66. Prideaux, B. *et al.* High-sensitivity MALDI-MRM-MS imaging of moxifloxacin distribution in tuberculosis-infected rabbit lungs and granulomatous lesions. *Anal. Chem.* **83,** 2112–2118 (2011).

67. Heien, M. L., Piehowski, P. D., Winograd, N. & Ewing, A. G. Lipid detection, identification, and imaging single cells with SIMS. *Methods Mol. Biol.* **656,** 85–97 (2010).

68. Moro, A. J., Cywinski, P. J., Korsten, S. & Mohr, G. J. An ATP fluorescent chemosensor based on a Zn(II)-complexed dipicolylamine receptor coupled with a naphthalimide chromophore. *Chem. Commun. (Camb).* **46,** 1085–1087 (2010).

69. Kurishita, Y., Kohira, T., Ojida, A. & Hamachi, I. Rational design of FRET-based ratiometric chemosensors for in vitro and in cell fluorescence analyses of nucleoside polyphosphates. *J. Am. Chem. Soc.* **132,** 13290–13299 (2010).

70. Huang, W. E., Li, M., Jarvis, R. M., Goodacre, R. & Banwart, S. A. Shining light on the microbial world the application of Raman microspectroscopy. *Adv. Appl. Microbiol.* **70,** 153–186 (2010).

71. Nasse, M. J. *et al.* High-resolution Fourier-transform infrared chemical imaging with multiple synchrotron beams. *Nat. Methods* **8,** 413–416 (2011).

72. Sauer, U. Metabolic networks in motion: 13C-based flux analysis. *Mol Syst Biol* **2,** 62 (2006).

73. Wiechert, W., Mollney, M., Isermann, N., Wurzel, M. & de Graaf, A. A. Bidirectional reaction steps in metabolic networks: III. Explicit solution and analysis of isotopomer labeling systems. *Biotechnol Bioeng* **66,** 69–85 (1999).

74. Metallo, C. M., Walther, J. L. & Stephanopoulos, G. Evaluation of 13C isotopic tracers for metabolic flux analysis in mammalian cells. *J Biotechnol* **144,** 167–174 (2009).

75. Duckwall, C. S., Murphy, T. A. & Young, J. D. Mapping cancer cell metabolism with(13)C flux analysis: Recent progress and future challenges. *J Carcinog* **12,** 13

(2013).

76. Wiechert, W., Schweissgut, O., Takanaga, H. & Frommer, W. B. Fluxomics: mass spectrometry versus quantitative imaging. *Curr. Opin. Plant Biol.* **10,** 323–330 (2007).

77. vanGulik, W. M., Antoniewicz, M. R., deLaat, W. T., Vinke, J. L. & Heijnen, J. J. Energetics of growth and penicillin production in a high-producing strain of Penicillium chrysogenum. *Biotechnol. Bioeng.* **72,** 185–193 (2001).

78. Kaplon, J., van Dam, L. & Peeper, D. Two-way communication between the metabolic and cell cycle machineries: the molecular basis. *Cell Cycle* **14,** 2022–2032 (2015).

79. Blagosklonny, M. V. & Pardee, A. B. The restriction point of the cell cycle. *Cell cycle (Georgetown, Tex.)* **1,** 103–110 (2002).

80. Banko, M. R. *et al.* Chemical genetic screen for AMPKalpha2 substrates uncovers a network of proteins involved in mitosis. *Mol Cell* **44,** 878–892 (2011).

81. Cuyàs, E., Corominas-Faja, B., Joven, J. & Menendez, J. A. in *Methods in molecular biology (Clifton, N.J.)* **1170,** 113–144 (2014).

82. Fingar, D. C. & Blenis, J. Target of rapamycin (TOR): an integrator of nutrient and growth factor signals and coordinator of cell growth and cell cycle progression. *Oncogene* **23,** 3151–3171 (2004).

83. Wellen, K. E. *et al.* ATP-citrate lyase links cellular metabolism to histone acetylation. *Science (80-.).* **324,** 1076–1080 (2009).

84. Sutendra, G. *et al.* A nuclear pyruvate dehydrogenase complex is important for the generation of Acetyl-CoA and histone acetylation. *Cell* **158,** 84–97 (2014).

85. Li, B., Carey, M. & Workman, J. L. The Role of Chromatin during Transcription. *Cell* **128,** 707–719 (2007).

86. Berger, S. L. The complex language of chromatin regulation during transcription. *Nature* **447,** 407–412 (2007).

87. Yalcin, A. *et al.* Nuclear targeting of 6-phosphofructo-2-kinase (PFKFB3) increases proliferation via cyclin-dependent kinases. *J Biol Chem* **284,** 24223–24232 (2009).

88. Yang, W. *et al.* ERK1/2-dependent phosphorylation and nuclear translocation of PKM2 promotes the Warburg effect. *Nat Cell Biol* **14,** 1295–1304 (2012).

89. Yang, W. *et al.* Nuclear PKM2 regulates β-catenin transactivation upon EGFR activation. *Nature* **478,** 118–122 (2011).

90. Estevez-Garcia, I. O. *et al.* Glucose and glutamine metabolism control by APC and SCF during the G1-to-S phase transition of the cell cycle. *J Physiol Biochem* **70,** 569–581 (2014).

91. Tudzarova, S. *et al.* Two ubiquitin ligases, APC/C-Cdh1 and SKP1-CUL1-F (SCF)-beta-TrCP, sequentially regulate glycolysis during the cell cycle. *Proc Natl Acad Sci U S A* **108,** 5278–5283 (2011).

92. Almeida, A., Bolanos, J. P. & Moncada, S. E3 ubiquitin ligase APC/C-Cdh1 accounts for the Warburg effect by linking glycolysis to cell proliferation. *Proc Natl Acad Sci U S A* **107,** 738–741 (2010).

93. Bienvenu, F. *et al.* Transcriptional role of cyclin D1 in development revealed by a genetic-proteomic screen. *Nature* **463,** 374–378 (2010).

94. Hsieh, M. C. F., Das, D., Sambandam, N., Zhang, M. Q. & Nahlé, Z. Regulation of the PDK4 isozyme by the Rb-E2F1 complex. *J. Biol. Chem.* **283,** 27410–27417 (2008).

95. Levine, A. J. & Puzio-Kuter, A. M. The control of the metabolic switch in cancers by oncogenes and tumor suppressor genes. *Science* **330,** 1340–1344 (2010).

96. Keyomarsi, K., Sandoval, L., Band, V. & Pardee, A. B. Synchronization of tumor and normal cells from G1 to multiple cell cycles by lovastatin. *Cancer Res.* **51,** 3602–3609 (1991).

97. Hengst, L., Dulic, V., Slingerland, J. M., Lees, E. & Reed, S. I. A cell cycle-regulated inhibitor of cyclin-dependent kinases. *Proc. Natl. Acad. Sci. U. S. A.* **91,** 5291–5295 (1994).

98. Lalande, M. A reversible arrest point in the late G1 phase of the mammalian cell cycle. *Exp. Cell Res.* **186,** 332–339 (1990).

99. Kalejta, R. F. & Hamlin, J. L. The dual effect of mimosine on DNA replication. *Exp. Cell Res.* **231,** 173–183 (1997).

100. BOOTSMA, D., BUDKE, L. & VOS, O. STUDIES ON SYNCHRONOUS DIVISION OF TISSUE CULTURE CELLS INITIATED BY EXCESS THYMIDINE. *Exp. Cell Res.* **33,** 301–309 (1964).

101. Adams, R. L. & Lindsay, J. G. Hydroxyurea reversal of inhibition and use as a cell-synchronizing agent. *J. Biol. Chem.* **242,** 1314–1317 (1967).

102. Ikegami, S. *et al.* Aphidicolin prevents mitotic cell division by interfering with the activity of DNA polymerase-alpha. *Nature* **275,** 458–460 (1978).

103. TAYLOR, E. W. THE MECHANISM OF COLCHICINE INHIBITION OF MITOSIS. I. KINETICS OF INHIBITION AND THE BINDING OF H3-COLCHICINE. *J. Cell Biol.* **25,** SUPPL:145-60 (1965).

104. Romsdahl, M. M. Synchronization of human cell lines with colcemid. *Exp. Cell Res.*

50, 463–467 (1968).

105. Zieve, G. W., Turnbull, D., Mullins, J. M. & McIntosh, J. R. Production of large numbers of mitotic mammalian cells by use of the reversible microtubule inhibitor nocodazole. Nocodazole accumulated mitotic cells. *Exp. Cell Res.* **126,** 397–405 (1980).

106. Langan, T. J. & Chou, R. C. Synchronization of mammalian cell cultures by serum deprivation. *Methods Mol. Biol.* **761,** 75–83 (2011).

107. Campisi, J., Morreo, G. & Pardee, A. B. Kinetics of G1 transit following brief starvation for serum factors. *Exp. Cell Res.* **152,** 459–466 (1984).

108. Rosner, M. & Hengstschlager, M. Nucleocytoplasmic localization of p70 S6K1, but not of its isoforms p85 and p31, is regulated by TSC2/mTOR. *Oncogene* **30,** 4509–4522 (2011).

109. Polyak, K. *et al.* p27Kip1, a cyclin-Cdk inhibitor, links transforming growth factor-beta and contact inhibition to cell cycle arrest. *Genes Dev.* **8,** 9–22 (1994).

110. Haberichter, T. *et al.* A systems biology dynamical model of mammalian G1 cell cycle progression. *Mol. Syst. Biol.* **3,** 84 (2007).

111. Juan, G., Hernando, E. & Cordon-Cardo, C. Separation of live cells in different phases of the cell cycle for gene expression analysis. *Cytometry* **49,** 170–175 (2002).

112. Schorl, C. & Sedivy, J. M. Analysis of cell cycle phases and progression in cultured mammalian cells. *Methods* **41,** 143–150 (2007).

113. Elvin, P. & Evans, C. W. Cell adhesiveness and the cell cycle: correlation in synchronized Balb/c 3T3 cells. *Biol. cell* **48,** 1–9 (1983).

114. Chen, Z., Odstrcil, E. A., Tu, B. P. & McKnight, S. L. Restriction of DNA replication to

the reductive phase of the metabolic cycle protects genome integrity. *Science (80-.).* **316,** 1916–1919 (2007).

115. Colombo, S. L. *et al.* Molecular basis for the differential use of glucose and glutamine in cell proliferation as revealed by synchronized HeLa cells. *Proc Natl Acad Sci U S A* **108,** 21069–21074 (2011).

116. Shaw, J., Payer, K., Son, S., Grover, W. H. & Manalis, S. R. A microfluidic 'baby machine' for cell synchronization. *Lab Chip* **12,** 2656–2663 (2012).

117. Tzur, A., Kafri, R., LeBleu, V. S., Lahav, G. & Kirschner, M. W. Cell Growth and Size Homeostasis in Proliferating Animal Cells. *Science (80-.).* **325,** 167 LP-171 (2009).

118. Davey, H. M. & Kell, D. B. Flow cytometry and cell sorting of heterogeneous microbial populations: the importance of single-cell analyses. *Microbiol. Rev.* **60,** 641–696 (1996).

119. Shen-Orr, S. S. & Gaujoux, R. Computational deconvolution: extracting cell type-specific information from heterogeneous samples. *Curr. Opin. Immunol.* **25,** 571–578 (2013).

120. Siegal-Gaskins, D., Ash, J. N. & Crosson, S. Model-Based Deconvolution of Cell Cycle Time-Series Data Reveals Gene Expression Details at High Resolution. *PLOS Comput. Biol.* **5,** e1000460 (2009).

121. Orlando, D. A., Iversen, E. S., Hartemink, A. J. & Haase, S. B. A BRANCHING PROCESS MODEL FOR FLOW CYTOMETRY AND BUDDING INDEX MEASUREMENTS IN CELL SYNCHRONY EXPERIMENTS. *Ann. Appl. Stat.* **3,** 1521–1541 (2009).

122. Oredsson, S. M. Polyamine dependence of normal cell-cycle progression. *Biochem. Soc. Trans.* **31,** 366–370 (2003).

123. Gaglio, D., Soldati, C., Vanoni, M., Alberghina, L. & Chiaradonna, F. Glutamine deprivation induces abortive s-phase rescued by deoxyribonucleotides in k-ras transformed fibroblasts. *PLoS One* **4,** e4715 (2009).

124. Yuan, J., Bennett, B. D. & Rabinowitz, J. D. Kinetic flux profiling for quantitation of cellular metabolic fluxes. *Nat Protoc* **3,** 1328–1340 (2008).

125. Fan, J. *et al.* Glutamine-driven oxidative phosphorylation is a major ATP source in transformed mammalian cells in both normoxia and hypoxia. *Mol Syst Biol* **9,** 712 (2013).

126. Fendt, S.-M. *et al.* Reductive glutamine metabolism is a function of the α-ketoglutarate to citrate ratio in cells. *Nat. Commun.* **4,** 2236 (2013).

127. Noh, K., Wahl, A. & Wiechert, W. Computational tools for isotopically instationary 13C labeling experiments under metabolic steady state conditions. *Metab Eng* **8,** 554–577 (2006).

128. Noack, S., Noh, K., Moch, M., Oldiges, M. & Wiechert, W. Stationary versus non-stationary (13)C-MFA: a comparison using a consistent dataset. *J Biotechnol* **154,** 179–190 (2011).

129. Vizan, P. *et al.* Modulation of pentose phosphate pathway during cell cycle progression in human colon adenocarcinoma cell line HT29. *Int J Cancer* **124,** 2789–2796 (2009).

130. Costenoble, R. *et al.* 13C-Labeled metabolic flux analysis of a fed-batch culture of elutriated Saccharomyces cerevisiae. *FEMS Yeast Res.* **7,** 511–526 (2007).

131. Sung, H. J. *et al.* Mitochondrial respiration protects against oxygen-associated DNA damage. *Nat. Commun.* **1,** 5 (2010).

132. Mitra, K., Wunder, C., Roysam, B., Lin, G. & Lippincott-Schwartz, J. A hyperfused mitochondrial state achieved at G1-S regulates cyclin E buildup and entry into S phase. *Proc. Natl. Acad. Sci. U. S. A.* **106,** 11960–5 (2009).

133. Olsen, J. V *et al.* Quantitative phosphoproteomics reveals widespread full phosphorylation site occupancy during mitosis. *Sci Signal* **3,** ra3 (2010).

134. Park, J. O. *et al.* Metabolite concentrations, fluxes and free energies imply efficient enzyme usage. *Nat. Chem. Biol.* **advance on,** 482–489 (2016).

135. Fell, D. Understanding the control of metabolism. *Front. Metab.* **2,** 300 (1997).

136. Metallo, C. M. *et al.* Reductive glutamine metabolism by IDH1 mediates lipogenesis under hypoxia. *Nature* **481,** 380–384 (2012).

137. Mullen, A. R. *et al.* Reductive carboxylation supports growth in tumour cells with defective mitochondria. *Nature* **481,** 385–388 (2012).

138. Jiang, L. *et al.* Reductive carboxylation supports redox homeostasis during anchorage-independent growth. *Nature* **532,** 255–258 (2016).

139. Saqcena, M. *et al.* Blocking anaplerotic entry of glutamine into the TCA cycle sensitizes K-Ras mutant cancer cells to cytotoxic drugs. *Oncogene* **34,** 2672–2680 (2015).

140. Diaz-Moralli, S., Tarrado-Castellarnau, M., Miranda, A. & Cascante, M. Targeting cell cycle regulation in cancer therapy. *Pharmacol Ther* **138,** 255–271 (2013).

141. Bennett, B. D., Yuan, J., Kimball, E. H. & Rabinowitz, J. D. Absolute quantitation of intracellular metabolite concentrations by an isotope ratio-based approach. *Nat Protoc* **3,** 1299–1311 (2008).

142. Clasquin, M. F., Melamud, E. & Rabinowitz, J. D. LC-MS data processing with

MAVEN: a metabolomic analysis and visualization engine. *Curr Protoc Bioinforma.* **Chapter 14,** Unit14 11 (2012).

143. Antoniewicz, M. R., Kelleher, J. K. & Stephanopoulos, G. Determination of confidence intervals of metabolic fluxes estimated from stable isotope measurements. *Metab Eng* **8,** 324–337 (2006).

אפיון המטבוליזם התאי לאורך מחזור התא בסרטן:

שיטה משולבת חישובית-ניסויית

חיבור על מחקר

לשם מילוי חלקי של הדרישות לקבלת התואר דוקטור לפילוסופיה

אן אויניונג

הוגש לסנט הטכניון- מכון טכנולוגי לישראל

חשון תשע"ט, חיפה, אוקטובר 2018